Mechanical, electrochemical and permeability behaviour of Ti6Al–4V scaffolds fabricated by electron beam powder bed fusion for orthopedic implant applications: The role of cell type

Original
Mechanical, electrochemical and permeability behaviour of Ti6Al–4V scaffolds fabricated by electron beam powder bed fusion for orthopedic implant applications: The role of cell type and cell size / Sichani, Hesam Rezvani; Atapour, Masoud; Ashrafizadeh, Fakhreddin; Galati, Manuela; Saboori, Abdollah. - In: JOURNAL OF MATERIALS RESEARCH AND TECHNOLOGY. - ISSN 2238-7854. - 28:(2024), pp. 3240-3257. [10.1016/j.jmrt.2023.12.260]

Publisher:
Elsevier Editora Ltda

Published
DOI:10.1016/j.jmrt.2023.12.260

Journal of Materials Research and Technology 28 (2024) 3240–3257

Contents lists available at ScienceDirect

Journal of Materials Research and Technology

journal homepage: www.elsevier.com/locate/jmrt

Mechanical, electrochemical and permeability behaviour of Ti6Al–4V scaffolds fabricated by electron beam powder bed fusion for orthopedic implant applications: The role of cell type and cell size

Hesam Rezvani Sichani [a], Masoud Atapour [a,**], Fakhreddin Ashrafizadeh [a], Manuela Galati [b], Abdollah Saboori [b,*]

[a] *Department of Materials Engineering, Isfahan University of Technology, Isfahan 84156-83111, Iran*
[b] *Integrated Additive Manufacturing Center, Department Management and Production Engineering, Politecnico di Torino, Torino, Italy*

ARTICLE INFO

Handling editor: P.Y. Chen

Keywords:
Ti-6Al–4V scaffolds
Electron beam powder bed fusion
Orthopedic implants
Mechanical properties
Permeability
Short/long-term corrosion

ABSTRACT

Ti–6Al–4V scaffolds have attracted much attention for biomedical applications owing to their bone-mimicking mechanical properties and better bone tissue in-growth and additive manufacturing can be employed to fabricate complex geometry scaffolds. The present study aimed to investigate the effects of scaffold architecture on the mechanical, electrochemical, and permeability behaviour of Ti–6Al–4V scaffolds fabricated by electron beam powder bed fusion (EB-PBF). For this, scaffolds with diamond and rhombic dodecahedron cell types, having various cell sizes, were designed and successfully fabricated. Chemical etching minimized the surface defects and improved the geometric fidelity of the scaffolds compared to the original designs. The larger the cell size, the coarser the dual α/β phase microstructure due to the higher heat accumulation in thicker struts. The scaffold architecture proved significant effects on the mechanical properties, where all scaffolds were mechanically comparable with human bone. Short/long-term electrochemical corrosion tests indicated that the corrosion performance significantly improved with an increase in cell size, irrespective of the cell type; this was attributed to the lower exposure of surface area to the electrolyte, coarse microstructure and a higher fraction of β phase. This study recommended that the EB-PBF Ti–6Al–4V scaffolds are promising candidates for orthopaedic implant applications from mechanical and electrochemical points of view.

1. Introduction

Over the last few decades, various processes have been developed to fabricate scaffolds with targeted geometry to mimic the mechanical behaviour of bone. Nowadays, special attention is paid to additive manufacturing (AM) techniques as an emerging and promising method that provides fast ways to fabricate metallic scaffolds [1–5]. Electron beam powder bed fusion (EB-PBF), which is commonly called electron beam melting (EBM), is able to manufacture complex scaffolds using an electron beam as the heat source to melt metallic powder in a layer-by-layer manner [6–10]. In this regard, various regular strut-based lattices like cubic, diamond, rhombic dodecahedron, and octahedral have been fabricated using EB-PBF, making them desirable scaffolds for biomedical applications [6,7,11,12]. Moreover, triply periodic minimal surfaces (TPMS), including the Schwarz gyroid, sheet gyroid, Schwarz primitive, and Schwarz diamond, have recently gained prominence in the fabrication of porous structures. These TPMS-based designs have been considered as promising designs for scaffold development [13]. Notably, researchers such as Yánez et al. [14], Koptyug et al. [13,15], Polley et al. [16], and Ataee et al. [6] have successfully manufactured TPMS-based Ti–6Al–4V porous structures using EB-PBF. These structures exhibit favourable mechanical properties and promote bone tissue ingrowth. As a result of these efforts, the scaffolds have been designed to possess the mechanical properties close to the bone to prevent stress shielding, osteopenia, and bone fracture and serve ideally for a long time or a lifetime without failure or re-surgery. This opens up broad clinical applications for AM scaffolds [16–19]. However, to attain minimal risk to patients' health, fabricating newly designed scaffolds to improve the

---

* Corresponding author.
** Corresponding author.
E-mail addresses: h.rezvanisichani@ma.iut.ac.ir (H.R. Sichani), m.atapour@cc.iut.ac.ir (M. Atapour), ashrafif@cc.iut.ac.ir (F. Ashrafizadeh), manuela.galati@polito.it (M. Galati), abdollah.saboori@polito.it (A. Saboori).

https://doi.org/10.1016/j.jmrt.2023.12.260
Received 30 August 2023; Received in revised form 18 December 2023; Accepted 27 December 2023
Available online 29 December 2023

scaffold's performance is still a hot spot in biomedical applications for future works. It was found that three main factors play the most critical roles in determining the scaffold's performance: (i) The materials they are made of, (ii) the geometry of scaffolds, and (iii) the relative density. In fact, scaffold geometry, including cell type, cell size, pore size, and porosity, plays a significant role in modifying the scaffolds to make mechanical properties comparable to bone [7,20–23]. In addition, geometry-related parameters must be optimized to provide a good biological response and adjust the tissue regeneration rate. Clearly, the more the porosity and the pore size are, the better bone ingrowth is achieved; however, there are limitations for the upper limit of these design parameters, driven by the need for sufficient mechanical strength consistent with the implantation site [24,25].

Considerable endeavours have been made to understand the architecture of scaffolds to mimic the mechanical properties of bone [6,20,22,26–28]. However, it is proved that the human body acts like an aqueous solution due to the various ions. Hence, corrosion performance is well known as one of the most important criteria for biomedical applications, especially from the release of harmful ions and biological responses points of view. This is of significant importance for scaffolds, having a very large surface area exposed to the electrolyte [29–32]. Therefore, well-designed scaffolds require an optimum architecture to satisfy the mechanical properties together with an acceptable performance from the corrosion point of view. However, a significant research gap exists concerning the simultaneous investigation of the interplay between corrosion and mechanical behaviour in AM Ti–6Al–4V scaffolds for biomedical applications. Limited research has delved into the concurrent examination of mechanical and corrosion behaviours of scaffolds, and they have not only assessed the short-term corrosion behaviour of scaffolds but also focused on scaffolds fabricated through laser powder bed fusion (LPBF) [33]. Accordingly, this work sought to evaluate the effects of scaffold architecture on the mechanical, electrochemical, and permeability characteristics of Ti–6Al–4V scaffolds fabricated by EB-PBF. Additionally, as yet an unclear issue, the long-term corrosion performance of EB-PBF Ti–6Al–4V scaffolds in biological environments, which is a decisive parameter in the biocompatibility of Ti-based implants, was also examined.

2. Materials and methods

2.1. Materials

Extra-low interstitials (ELI) grade Arcam Ti–6Al–4V powder was used as a feedstock material for the EB-PBF process. The chemical composition of the Arcam powder is listed in Table 1. Fig. 1 indicates the morphology and particle size distribution of the initial Ti–6Al–4V powder. The scanning electron microscopy (SEM) analysis confirmed that the Ti–6Al–4V powder displayed a spherical shape and smooth surface, ensuring excellent flowability for a successful EB-PBF process. The particle size distribution, determined via image analysis, revealed D (10), D(50), and D(90) values of 50 μm, 66 μm, and 85 μm, respectively, as illustrated in Fig. 1 (b). This indicates that particles smaller than 50 μm constitute less than 10 % of the total. In practical terms, the Ti–6Al–4V powder showed a particle diameter ranging from 45 μm to 106 μm, with an average size of approximately 75 μm.

2.2. Design and EB-PBF manufacturing

In the present study, two scaffolds with different cell types and cell sizes ((I) Rhombic Dodecahedron (RD, 3 mm, 5 mm) and (II) Diamond (DO, 3 mm, 5 mm)) were designed based on the database of the Materialise Magics 21.11 using computer-assisted design (CAD) software, as shown in Fig. 2. Accordingly, the scaffolds were called RD3, RD5, DO3, and DO5, where the letters designate the cell type and the number indicates the cell size. This design of experiments was employed to investigate the effects of cell type and cell size on the performance of EB-PBF Ti–6Al–4V scaffolds. It is noteworthy that the thickness of struts in different samples was chosen in such a way that the porosity of all samples remains the same (~80 %). Based on designed models, the surface area, as an important factor for scaffolds performance, series in sequence as follows: RD3 (5268.31 mm^2) > DO3 (3958.88 mm^2) > RD5 (3013.85 mm^2) > DO5 (2770.59 mm^2).

All scaffolds with a cubic shape with a dimension of 15 × 15 × 15 mm^3 were fabricated by an Arcam A2X machine. Afterwards, the samples were naturally cooled down inside the EB-PBF chamber to room temperature. The EB-PBF process parameters employed in the present study are shown in Table 2. All samples were successfully additively manufactured using the EB-PBF process and are macroscopically represented in Fig. 3, indicating a regular pore size and shape arrangement for all samples. The designed CAD models were compared with the as-built scaffolds, and the geometrical characteristics are summarized in Table 3. It can be seen that the Ti–6Al–4V scaffolds were reasonably similar with respect to the CAD design in terms of geometrical fidelity. To eliminate any remaining loose powder and sintered particles, a standard post-processing procedure following EB-PBF was employed. Initially, all as-built samples underwent blasting using ELI Ti–6Al–4V powder [34,35]. Subsequently, these blasted samples were subjected to chemical etching by immersion in a solution containing 2 ml of HF, 20 ml of HNO_3, and 78 ml of H_2O. Notably, the required etching time correlated with the complexity of the cell structure and the reduction in cell size. During the chemical etching process, the samples were fully immersed in the specified etchant solution, with continuous stirring facilitated by a conventional magnetic stirrer. We have tried to enhance the penetration of the etchant into the internal lattice of the samples. Consequently, the etching times for RD3, DO3, RD5, and DO5 were determined as 19, 15, 11, and 10 min, respectively. Additionally, regardless of the cell type and size, all samples underwent a final rinse with deionized water using bench-top ultrasonic cleaners for a duration of 10 min.

2.3. Characterization of as-built scaffolds

The microstructural investigations of fabricated Ti–6Al–4V scaffolds were performed by X-ray diffraction (XRD, Philips X'PERT diffractometer, Cu Kα radiation: $\lambda = 1.542$ Å at 20 kV and 30 mA) and scanning electron microscopy (SEM, Philips XL30) equipped with energy-dispersive x-ray spectroscopy (EDS). The samples were sectioned, mounted, well-grounded and mechanically polished using a conventional metallographic techniques, and etched by Kroll's reagent (2 ml HF + 6 ml HNO_3 + 92 ml distilled water) [32]. The surface roughness of struts before and after chemical etching was analyzed by a laser profilometer (Fanavari Kahroba Co., vertical resolution = 1 μm); for each specimen. It is essential to emphasize that measurements were obtained from eight distinct interior and exterior struts of the scaffolds. The R_z parameter, which signifies the maximum peak-to-valley height across the surface, the R_q parameter, representing the root mean square deviation from the profile, and the R_a value, denoting the arithmetic mean deviation from the mean line, were all determined. The average of these

Table 1
Nominal chemical composition of the Arcam Ti–6Al–4V powder utilized in this study.

Ti–6Al–4V	Al	V	C	Fe	O	N	H	Ti
Standard (ELI)	5.5–6.5	3.5–4.5	<0.08	<0.25	<0.13	0.05	<0.012	Bal.
Arcam (ELI)	4.16	3.86	0.02	0.19	0.09	0.01	0.002	Bal.

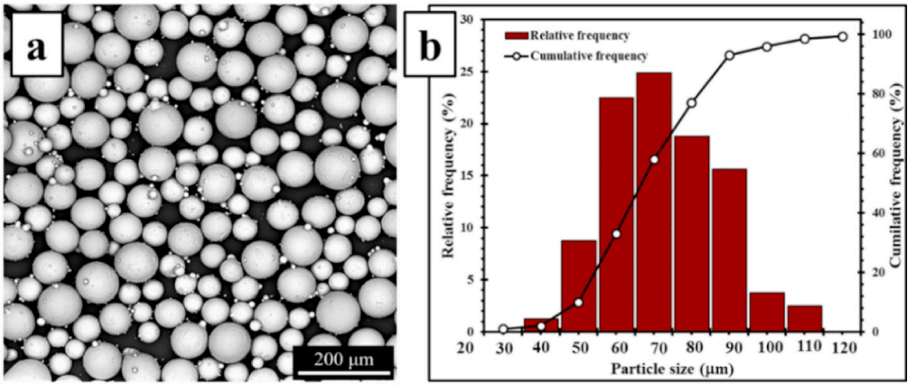

Fig. 1. (a) SEM morphology and (b) particle size distribution histograms of the initial Ti–6Al–4V powder.

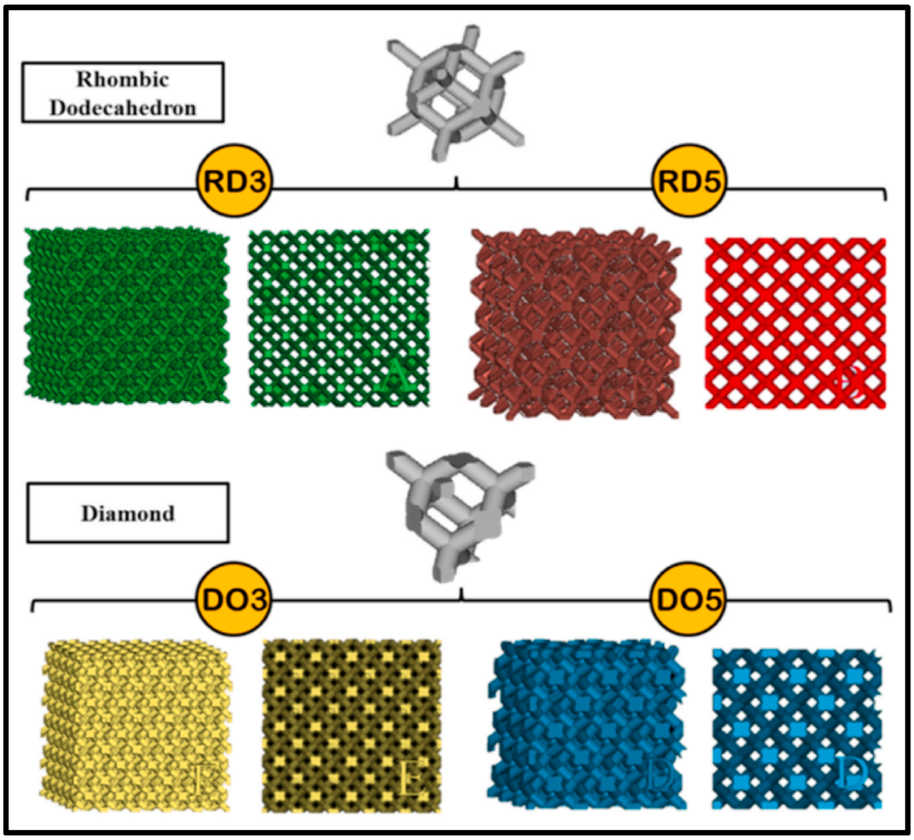

Fig. 2. The CAD models of Ti–6Al–4V scaffolds with different cell types and sizes.

Table 2
The EB-PBF process parameters used to fabricate the Ti–6Al–4V scaffolds.

Ti–6Al–4V	Scan speed (mm/s)	Focus offset (mA)	Max. Beam current (mA)	Number of contours	Hatch contour (mm)
Outer contour	450	0	3	1	0.13
Inner contour	470	0	3	1	0.19

parameters serves as an indicator of the roughness characteristics. To determine the porosity of the scaffolds, the Archimedes method [36] was performed five times, and the porosity (P) was also calculated with Eq. (1) based on scaffold volume [21].

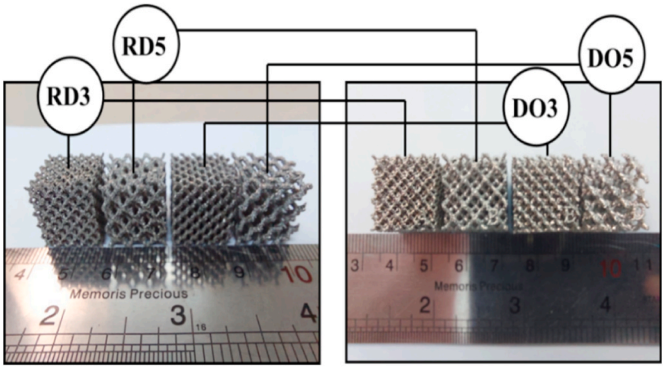

Fig. 3. The EB-PBF Ti–6Al–4V scaffolds with different cell types and sizes.

Table 3
Comparison of geometrical characteristics of EB-PBF Ti–6Al–4V samples with designed models.

The geometrical characteristics of the designed models					
Sample	**Dimensions (mm^3)**[a]	**Cell length (mm)**	**Porosity (%)**	**Strut thickness (mm)**	**Strut length (mm)**
RD3	15 × 15 × 15	3	80	0.5	1
RD5	15 × 15 × 15	5	80	0.74	2
DO3	15 × 15 × 15	3	80	0.60	2
DO5	15 × 15 × 15	5	80	1	2.22
Sample	**Average dimensions (mm^3)**	**Cell length (mm)**	**Porosity (%)**	**Strut thickness (mm)**	**Strut length (mm)**
The geometrical characteristics of the as-built models					
RD3	15.32 × 15.23 × 14.87	3	74.71 ± 2	0.64 ± 0.06	1.09 ± 0.02
RD5	15.34 × 15.38 × 14.83	5	78.85 ± 3	0.91 ± 0.08	2.11 ± 0.03
DO3	15.23 × 15.36 × 14.88	3	75.65 ± 2	0.72 ± 0.65	2.06 ± 0.06
DO5	15.30 × 15.28 × 14.85	5	78.59 ± 3	1.18 ± 0.11	2.30 ± 0.04

[a] The dimensions were reported in the order of X × Y × Z - axes (Z: the build direction).

$$P = 1 - \frac{V_P}{V} \tag{1}$$

where V_p and V are the volume of the scaffold and the volume of a solid cube, having the same size as the scaffold, respectively.

To evaluate the mechanical behaviour of Ti–6Al–4V lattice specimens, a uniaxial compression test was carried out at a fixed strain rate of 1 mm/min according to ISO 13314 standard [16,36]. During the compression test, the scaffolds were centrally placed between two steel plates and the test was continued until full densification of the structure. To minimize the effects of the build direction on the mechanical behaviour, all the samples were compressed along the printing direction (Z direction). The compression tests were recorded by a digital camera to determine the damage behaviour and failure modes. Stress-strain curves were drawn by the initial cross-sectional area of an assumed dense sample [16]. The absorbed energy up to the first failure, per unit volume of each structure (W_v), was determined with respect to the area enclosed by the compressive stress-strain curve and can be calculated as follow [7];

$$W_v = \int \sigma(\varepsilon) d\varepsilon \ . \ V^* \tag{2}$$

where σ and ε are the stress and strain, respectively. The V^* represents the mass of the structure to the nominal density of the Ti–6Al–4V (4.43 g/cm^3) ratio. The compression loading was performed three times for each sample. The reported mechanical characteristic values represent the averages obtained from these three compression tests for each individual sample. To determine the hardness of struts, the Vickers microhardness test was performed at the applied load of 100 g and dwell time of 10 s. The reported hardness is the average of five indentations on the struts for each mounted and polished sample.

To investigate the dynamic wettability of the samples, a 10 μL water droplet was carefully deposited by a microsyringe on the surface of the scaffolds. Time-lapse images of samples during wettability tests were recorded at different moments according to the cell type and size using a digital camera. The falling head method [21,37] was utilized to evaluate the permeability of fabricated scaffolds. To do so, a certain amount of water gradually dropped inside the standpipe from h_1 to h_2, which was constant for each sample. This test was repeated five times, and the average time value was adopted for permeability. The schematic of the experimental setup of permeability tests based on the falling head method is presented in Fig. 4 (a).

The permeability of Ti–6Al–4V scaffolds was inferred by Darcy's law and calculated as follows [37];

$$K = \frac{a}{A}\frac{L}{t_i - t_0} ln\frac{h_1\mu}{h_2\rho g} \tag{3}$$

where a, A, and L are the cross-sectional area of the standpipe, cross-sectional area and height of the sample, respectively. μ and ρ represent the viscosity and density of water, respectively, and are equal to 1.01×10^{-9} MPa s and 1 g/cm^3. The K can be calculated by integrating the water flow rate over the measurement time t_i-t_0 such that h_1 and h_2 are the initial height at t_0 and the final height at t_i, respectively. It is important to recognize that for a comprehensive understanding of the interaction mechanism between scaffold architecture and permeability behaviour, we investigated the pressure drop and permeability of the scaffolds across various flow rates. Specifically, we selected four distinct flow rates (0.004, 0.006, 0.008, and 0.01 m/s) to establish correlations between pressure drop, permeability, and the corresponding flow rate. Notably, the permeability values of the scaffolds were determined under specific conditions: the inlet-flow velocity was set at the mentioned flow rates, while the outlet pressure on the opposite-flow side remained at zero. Furthermore, the pressure drop (ΔP), which represents the difference in pressure from the inlet plane to the outlet plane, was calculated using the following equation [38]:

$$\Delta P = P_{inlet\ plane} \ - \ P_{outlet\ plane} \tag{4}$$

The permeability test was repeated five times, and the average time value was adopted for permeability. To assess the corrosion behaviour of the fabricated scaffolds, a conventional three-electrode system comprising a platinum electrode as a counter electrode, a commercial saturated Ag/AgCl as a reference electrode, and a fabricated Ti–6Al–4V scaffold as a working electrode was employed to measure the open circuit potential (OCP), potentiodynamic polarization, as well as electrochemical impedance spectroscopy (EIS). All in-vitro corrosion tests were carried out by means of PARASTAT 2273 electrochemical system (EG&G, USA) in phosphate-buffered saline (PBS, pH = 7.4) at 37 °C. The composition of the PBS solution is given in Table 4. It is noticeable that similar dimensions of all samples were exposed to PBS, and their surface area served as the working area. The schematic of the corrosion setup is shown in Fig. 4 (b). Before being subjected to corrosion testing, The as-built scaffolds underwent a degreasing process with acetone, followed by washing with deionized water using bench-top ultrasonic cleaners for

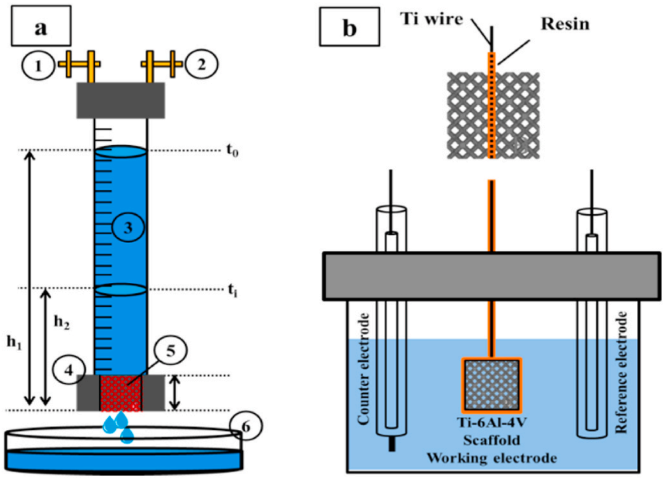

Fig. 4. (a) The schematic of the experimental setup of permeability tests based on the falling head method: (1) Air-valve, (2) Vacuum pump valve, (3) Standpipe, (4) Sample holder, (5) Ti–6Al–4V scaffold, (6) Water container. (b) Schematic drawing of the setup of corrosion tests.

Table 4
Composition of the PBS solution used in this study.

Component	NaCl	KCl	Na_2HPO_4	KH_2PO_4
Concentration ($g.L^{-1}$)	8	0.2	1.42	0.24

8 min. Subsequently, they were dried and immersed in fresh PBS for 12 h at 37 °C to allow the corrosion potential to stabilize. The OCP was continuously recorded over a period of 4000 s until changes were smaller than 50 mV/5 min. The EIS was performed at OCP in a frequency range from 10 mHz to 100 kHz with an amplitude of 1 mV and 36 points/dec.

All the experimental impedance data were fitted using an appropriate equivalent electrical circuit using the ZView® software (Scribner Associates Inc.). The potentiodynamic polarization was attained in the −250 mV versus E_{OCP} till the final potential of 1.90 V using a scan rate of 1 mV/s. The corrosion potential (E_{corr}), as a thermodynamic parameter, and corrosion current density (i_{corr}), representing the corrosion rate were determined by the Tafel extrapolation method. As one of the innovative aspects of the current study, the long-term corrosion performance of scaffolds was herein assessed after immersing in PBS at 37 °C for 1 d and 21 d, where the solution was completely replaced with fresh PBS every 7 d. The corrosion tests were repeated three times for each sample to ensure the correctness of output and data reproducibility. The ion release of Ti and V elements was detected from Ti–6Al–4V scaffolds during long-term immersion in 20 mL of the PBS solution at 37 °C using inductively coupled plasma mass spectroscopy (ICP-MS, USA). To do so, each sample was cleaned and dried prior to testing, and was hung vertically in the cylindrical tubes without touching the walls and bottom. The immersion tests were conducted for 3, 7, 14 and 21 d, respectively.

3. Results and discussion

3.1. Surface morphology of the Ti–6Al–4V scaffolds

SEM micrographs of the surface morphology of the Ti–6Al–4V scaffolds are presented in Fig. 5(a–d), indicating a rough surface of an individual strut, which is typical for EB-PBF parts in the as-built state. The surface contained weakly bounded/unmelted/partially melted powder particles attached to the scaffold surface, as an inherent feature of any powder-based system [39]. This even led to the thickness of the oversized struts compared to the designed dimensions, leading to a decrease in the measured pore size and porosity (Table 3). The findings showed that, regardless of cell type, the increase in the cell size caused more deviation in the strut thickness from the designed value. Studies showed

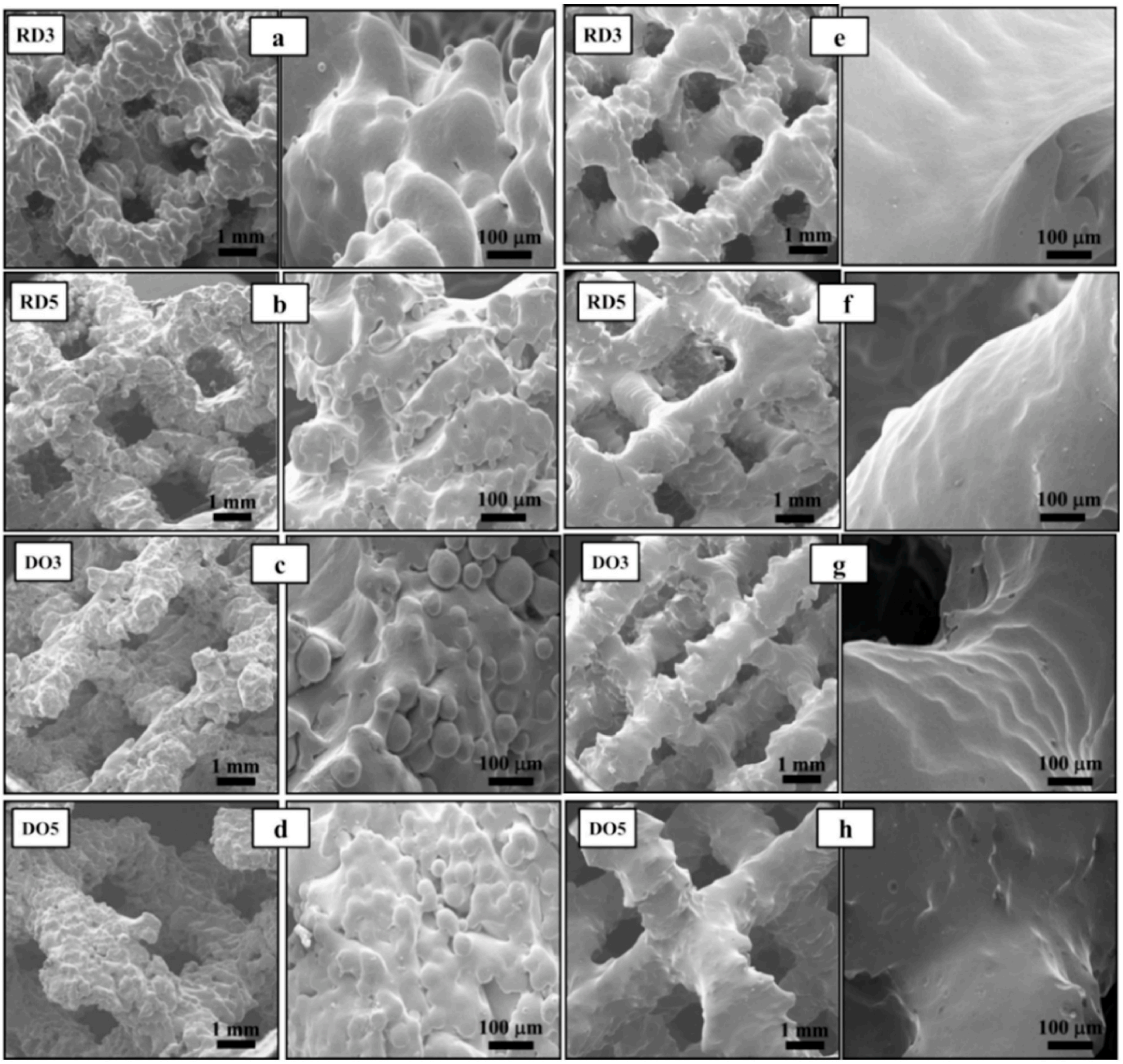

Fig. 5. SEM micrographs of EB-PBF Ti–6Al–4V scaffolds at different magnifications; (a–d) as-built conditions and (e–h) after chemical etching post-processing.

that, under similar EB-PBF parameters, as the strut thickness increased, more powder was attached to the strut surface. The reason for this may be attributed to the overall heat capacity of the built. As the sample thickness increases, it can store more heat energy, which serves as a repeated heat source for the sintering process in wider areas surrounding the struts. Surface roughness/topography is a key property of the material to be used as biomaterial. On one hand, the surface-attached powders can result in localized stress and crack initiation, significantly weakening the mechanical performance and life time of the scaffolds [40–43]. On the other hand, the impact of roughness induced by attached powder on the biological behaviour of scaffolds remains a topic of debate. Numerous studies have demonstrated that attached powder can either enhance human bone cell attachment and proliferation or pose risks by detaching from the implant surface [32,44,45]. Accordingly, in the present study, the as-built scaffolds were chemically etched to remove surface-attached powders from the scaffold's surface as much as possible. By doing this, the surface roughness/topography of all the scaffolds became almost similar; this would minimize the effects of the surface influencing parameters on the scaffold's properties. The surfaces of scaffolds after this post-processing treatment are shown in Fig. 5(e–h).

The surface roughness parameters—specifically R_a, R_q, and R_z—were measured for all scaffolds and summarized in Table 5 as comparable characteristics. As can be observed in Fig. 5, the overall surface quality of the samples was improved after etching; however, not all attached powder particles were completely removed from the surface of the scaffolds. From Tables 5 and it can be found that R_a decreased with respect to the as-built sample surface for all scaffolds after being etched. Surface modification of scaffolds by chemical etching strongly depends on etching time, etchant concentration, and the material from which the implant is made. Irrespective of other parameters, the etching time is of great importance to improve the surface quality of scaffolds; short-time etching was found to be insufficient for maximum removal of attached powder, and long-time etching can result in serious damage to struts, especially on low-thickness struts [34,46]. It appeared that the more complex the cell type and the smaller the cell size, the longer was the required etching time, which was trended in the following order: RD3 > DO3 > RD5 > DO5. It is clear that the cell size compared to the cell type has played a more decisive role in the chemical etching process because the increase in cell size accelerated the etchant movement and penetration throughout the scaffold and, as a result, the attached particles were removed in a shorter time. The etching time was adjusted to obtain an average roughness (R_a) in the range 14–26 μm for all scaffolds, as can be seen in Table 5.

3.2. Microstructure of the Ti–6Al–4V scaffolds

A hexagonally packed acicular martensitic phase microstructure (α′) is usually formed in the as-built Ti–6Al–4V alloy fabricated by the AM process, which stems from the nature of this technique as a rapid solidification process [47–51]. In the present study, however, the as-built Ti–6Al–4V samples fabricated via EB-PBF consisted of only α/β dual-phase microstructure, as shown in Fig. 6 (a). As can be distinguished in Fig. 6, the high-contrast phase region is enriched in heavy metals like vanadium, representing β phase and the other one is α phase, which is rich in aluminium, as confirmed by EDS analysis. This structure is considered to be favoured for titanium implant applications from the point of view of mechanical properties [6,52]. The α/β microstructure basically is a result of the thermal history experienced by Ti–6Al–4V powders, continuously undergoing a preheating–melting–cooling cycle during EB-PBF. The melting of the powder layers leads to the epitaxial growth of prior β phase grains during EB-PBF; the β grains tend to be elongated towards the temperature gradient, that is, the build-direction. With further cooling, the elevated temperature β phase can transform into a low-temperature α phase via a diffusion less mechanism when the temperature is reduced below β→α transition temperature. This might result in the formation of the martensitic α′-titanium phase, which grows inside the primary β columns in the form of dispersed lamellae. Nevertheless, considering that, in the EB-PBF process, the build chamber is kept at an elevated temperature of around 650–700 (C), the cooling rate is slow. For this reason, α′ phase is decomposed to α/β dual phase, which is typical for the diffusion transformation in Ti–6Al–4V alloy [7,35,53,54]. Many also suggested that, in EB-PBF, the cooling rate at the beginning of solidification is estimated to be about 10^3–10^5 °C/s, which is very high. Therefore, at this stage, the supersaturated α′ phase is formed and immediately decomposes into α/β phase at a temperature of about 587 °C [55]. In addition, it was suggested that α′ phase is also decomposed to α and β owing to the preheating step and/or reheating or partially re-melting the previously solidified layer when the electron beam melts the new layer during the EB-PBF process [7,56].

To understand more precisely, Fig. 6 (b) shows the schematic of the microstructure evolution of EB-PBF Ti–6Al–4V, involving α′ formation and decomposition to α/β. According to Fig. 6, microstructural analysis implies that cell type had no remarkable effect on the microstructure of the scaffolds. It can be observed that, regardless of cell type, the microstructure of the samples was rather identical for the same cell size. It is obvious that β spacing increases with an increase in the cell size (i.e. thicker struts). The larger the cell size, the coarser is the microstructure. This phenomenon can likely be attributed, drawing on prior research [40,41,57], to greater heat accumulation in thicker struts. Consequently, samples with larger cell sizes exhibit a slower cooling rate and a coarser microstructure. It is proved that the α/β interface, acting as a barrier against dislocation slips, plays an important role in the strengthening behaviour of EB-PBF Ti–6Al–4V alloys [56,58]. The XRD patterns of the EB-PBF Ti–6Al–4V scaffolds in Fig. 7 confirm the phase constituents consisting of a combination of α/β dual phase in the specimens.

3.3. Mechanical behaviour of Ti–6Al–4V scaffolds

Fig. 8 presents the stress-strain curves of EB-PBF Ti–6Al–4V scaffolds in compression tests; three distinct regions can be distinguished, as they are typical for porous metallic specimens [7,21,22]. In all cases, a linear elastic deformation region exists up to the first compressive strength peak, where the stress drop was closely related to the first failure of the scaffolds and the release of a large amount of energy. This region is followed by a plateau region characterized by stress fluctuations at a relatively constant stress. As shown in Fig. 8, the stress fluctuations of DO scaffolds at the plateau region are greater compared to RD scaffolds, independent of cell size. As the compressive load reached the ultimate strength of the scaffold layers, a larger number of load-bearing struts broke during each fracture event. This resulted in a significant and noticeable decrease in stress (stress drop) due to the increased number of broken struts. As a result, stress fluctuations increased around a specific

Table 5
Roughness parameters of EB-PBF Ti–6Al–4V scaffolds before and after chemical etching.

Samples	As-built conditions			After chemical etching		
	R_a (μm)[a]	R_q (μm)[b]	R_z (μm)[c]	R_a (μm)	R_q (μm)	R_z (μm)
RD3	85.26 ± 6	89.41 ± 7	356.18 ± 21	24.16 ± 4	26.75 ± 3	50.16 ± 7
RD5	96.18 ± 9	101.75 ± 9	461.14 ± 35	17.20 ± 3	20.05 ± 1	49.12 ± 4
DO3	76.16 ± 5	81.42 ± 8	304.44 ± 18	26.14 ± 5	25.94 ± 6	51.45 ± 8
DO5	100.30 ± 8	107.26 ± 12	525.31 ± 31	14.23 ± 4	16.84 ± 6	39.09 ± 6

[a] **R_a:** The arithmetic average of the absolute values of the roughness profile heights.
[b] **R_q:** The root mean square of the roughness profile heights.
[c] **R_z:** The maximum peak-to-valley height within a specified sampling length on the surface.

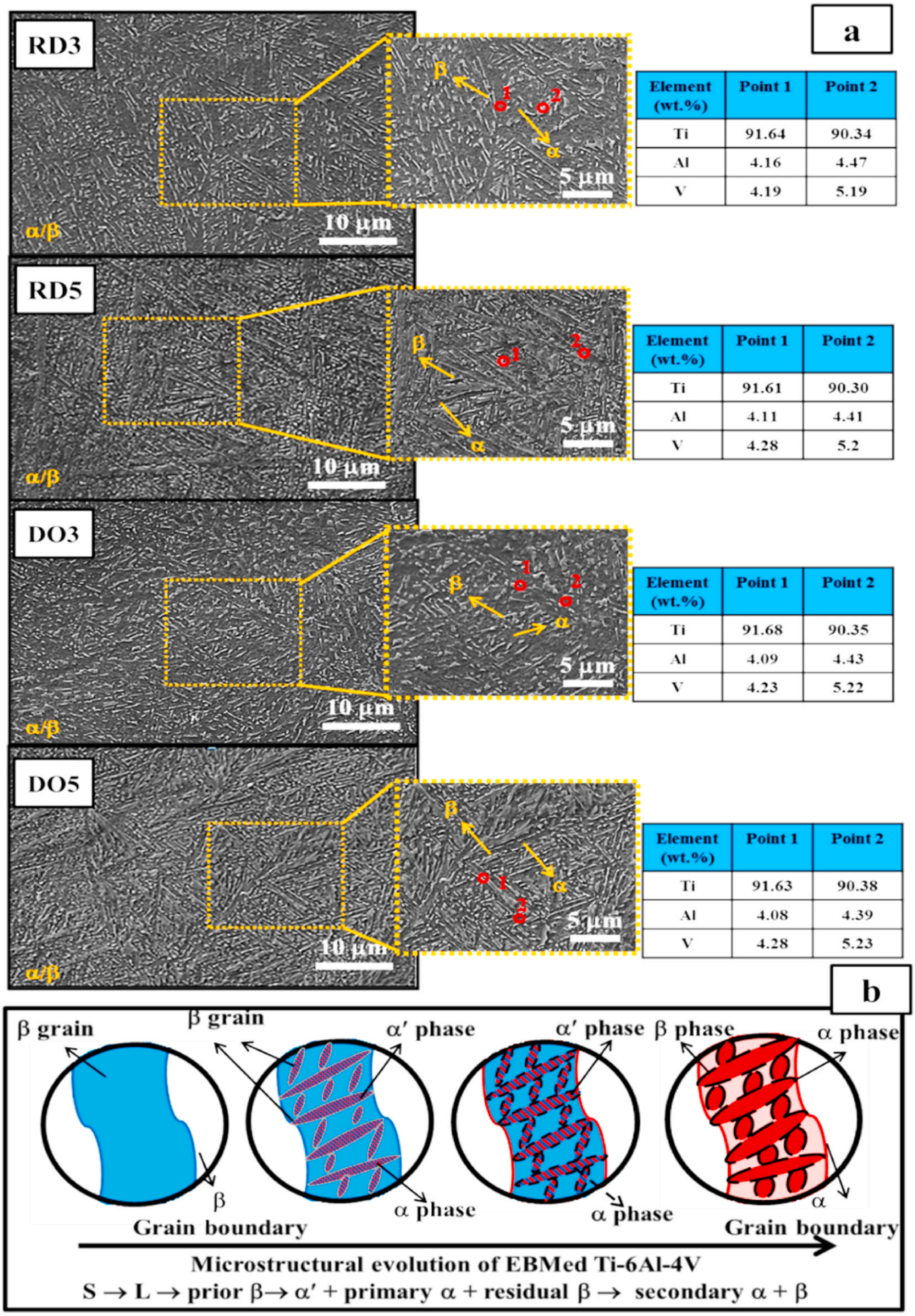

RD3

Element (wt.%)	Point 1	Point 2
Ti	91.64	90.34
Al	4.16	4.47
V	4.19	5.19

RD5

Element (wt.%)	Point 1	Point 2
Ti	91.61	90.30
Al	4.11	4.41
V	4.28	5.2

DO3

Element (wt.%)	Point 1	Point 2
Ti	91.68	90.35
Al	4.09	4.43
V	4.23	5.22

DO5

Element (wt.%)	Point 1	Point 2
Ti	91.63	90.38
Al	4.08	4.39
V	4.28	5.23

Fig. 6. (a) Microstructural features of the four types of EB-PBF Ti–6Al–4V scaffolds, (b) the illustrative depiction of the evolution of microstructure of EB-PBF Ti–6Al–4V.

stress. In addition, it can be found that the stresses in the plateau region do not exceed the maximum stress value corresponding to the first failure, indicating the higher energy absorption value of the scaffolds in the first failure compared to subsequent failures.

From Fig. 8, all of the stress-strain curves showed a densification region which is recognized by a rapid stress increase. The densification behaviour of a lattice structure is connected with its architecture and porosity in terms of strut thickness and pore size. Results indicated that densification occurred at lower strain for scaffolds with small cell sizes, regardless of the cell type. The reason can be explained as that for the scaffolds with large cell sizes, a large volume of fractured material continuously separated from the scaffolds during the compressive deformation, and the unbroken volume of the sample was mostly free of broken struts. Therefore, for large cell size, the total porosity of the

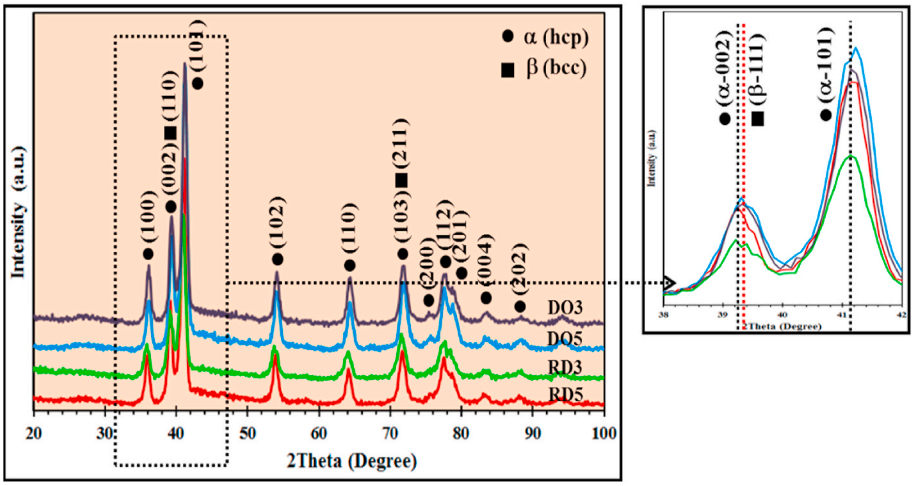

Fig. 7. (a) XRD patterns of the EB-PBF Ti–6Al–4V scaffolds.

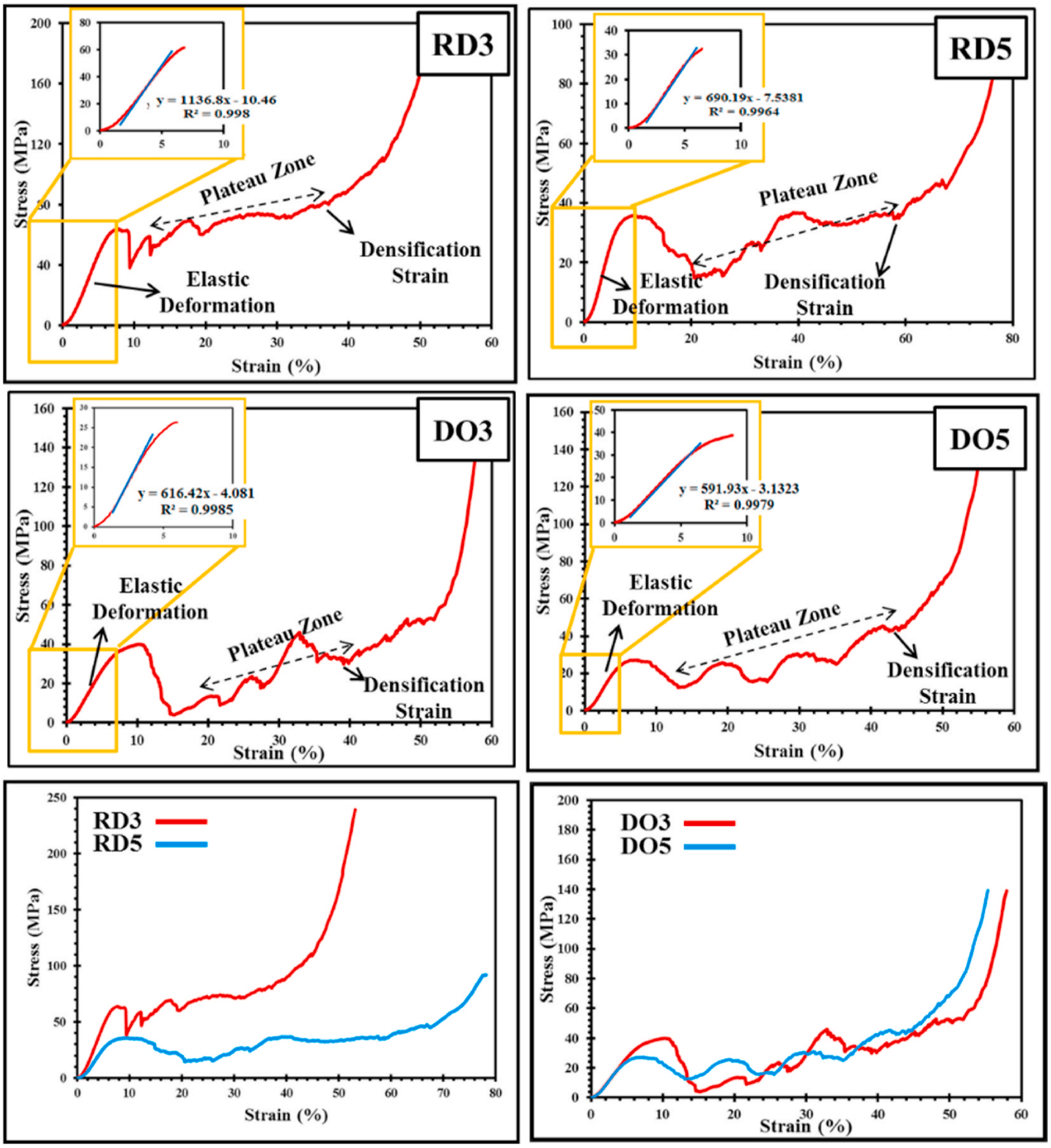

Fig. 8. The stress-strain curves under compressive loading for EB-PBF Ti–6Al–4V scaffolds, featuring various cell types and sizes.

scaffold was almost unvaried during the compressive loading. This is while, for the scaffolds with small cell size, the porosity of the structure gradually reduced owing to the remaining broken struts in the unbroken volume, thus giving rise to earlier densification [21]. The mechanical characteristics of EB-PBF Ti–6Al–4V scaffolds were extracted based on the ISO 13314 [36] and are given in Table 6, where σ_{max} represents the maximum compressive strength at the first failure and $\sigma_{Plateau}$ corresponds to the mean value of the stress at plateau region of the curve. Notably, the first maximum compressive strength is commonly defined as the ultimate compressive strength (UCS). Obvious differences are observed in the mechanical properties of the scaffolds with different designed architectures.

From Table 6, considering the same cell size, the RD scaffolds exhibited better mechanical properties than DI scaffolds in terms of elastic modulus, yield stress, and ultimate stress. The UCS of RD3 and RD5 were measured at approximately 68 MPa and 39 MPa, respectively, which are ~70 % and ~48 % greater than that of DO3 and DO5. Additionally, the elastic moduli of RD3, 1.13 GPa, and RD5, 0.69 GPa, were higher than those of DO3, 0.61 GPa, and DO5, 0.59 GPa. Moreover, with the increase in cell size, the mechanical properties of the scaffolds were degraded, which is more evident in the RD structure. The mechanical performance of the scaffolds originated from the parent material properties, geometrical architecture, and microstructure. It seems that parameters related to geometry, including cell type, pore size, strut thickness, and porosity, play the most important role [20,59,60]. Here, the lower mechanical properties of RD scaffolds compared to DO scaffolds can be attributed to cell type; it is clear that RD scaffolds, due to their more complex cell, have more load-bearing struts in the entire scaffolds array, which is consistent for both cell sizes. Although the microstructure of scaffolds, which was dependent on the cell size, affected the mechanical behaviour, the scaffolds geometry caused more profound effects on the mechanical properties. The study confirmed that all the scaffolds were mechanically suitable for orthopaedic implant applications. Their elastic modulus was low enough to prevent stress shielding, while their mechanical strengths were sufficiently high to ensure stability. Notably, the EB-PBF Ti–6Al–4V scaffolds exhibited mechanical strength comparable to or greater than traditional similar lattice cell types reported in previous studies [61,62]. Although their Young's modulus is lower than that of similar lattice structures, it suggests their potential as an alternative design to mitigate stress shielding in orthopaedic implants. Interestingly, these existing structures not only possess Young's modulus compatible with trabecular bone but also exhibit a higher ultimate UCS than trabecular bone. Fig. 9 illustrates that the mechanical properties of the scaffolds fall within the range of human cortical and trabecular bone. Particularly, their mechanical characteristics closely resemble those of trabecular bone, making them a subject of significant interest among researchers for bone implantation [6,18,63].

It is also observed that, regardless of cell size, the energy absorption of RD scaffolds, up to the onset of failure, was greater than that of the DI scaffolds. This behaviour can be attributed to the greater number of main, load-bearing struts of the RD structures in the cell array located along the loading direction [64]. Correspondingly, the decrease in the cell size enhanced the energy absorption capacity.

The microhardness values of EB-PBF Ti–6Al–4V scaffolds were all in the same range and in agreement with EB-PBF Ti–6Al–4V samples reported in the literature; these are higher than the values for Ti–6Al–4V counterpart produced by SLM [6,65]. It is noteworthy that the hardness of Ti–6Al–4V scaffolds depends on the microstructure and strut thickness. The hardness would decrease with the decrease in strut thickness for EB-PBF Ti–6Al–4V scaffolds because a thicker strut provides more support to bear the indentation load. Moreover, it could be argued that the α/β interface induced by EB-PBF thermal history could be of importance in affecting the hardness. The coarser the microstructure, the lower is the hardness [35,66]. Hence, it can be concluded that the hardness herein was derived from the competition of these two factors.

3.4. Failure modes analysis of Ti–6Al–4V scaffolds

The failure modes of the four kinds of scaffolds were investigated to further understand the mechanical behaviour of the scaffolds. For that, the uniaxial compressive response of the as-built Ti–6Al–4V scaffolds was studied by a digital video recorder. The deformation process of all the scaffolds at the given compressive strain is shown in Fig. 10.

It can be observed that the samples exhibited different deformation behaviour during the compression process due to their designed architecture. The initial failure of RD3 occurred at an angle of approximately 45° to the loading axis, which is different from others. At the strain of 0.08, the 45° shear band (marked by a red rectangle) acted at the top region of RD3, where the load-bearing struts started to fracture, mirrored by the first stress drop in the stress-strain curve. With increasing compressive strain, the load-bearing struts fractured layer-by-layer at the 45° shear bands. This is while, unlike RD3, the failure initiated from the top layer of RD5 at a strain of 0.11, corresponding to the first stress drop in the stress-strain curve. As the compression loading continued, the failure region gradually expanded with the fracture of load-bearing struts in the form of layer-by-layer, corresponding to the stress fluctuations in the plateau region of the stress-strain curve. Unlike RD scaffolds, the DO scaffolds, regardless of their cell size, collapsed layer-by-layer from the bottom to the top layer. By analyzing the deformation behaviour of scaffolds during compression and examining the shape of thestress–strain curve, we observe distinct stress concentrations. Specifically, for RD5, stress accumulates predominantly at the top layers, while for DO3 and DO5, it concentrates at the bottom layers. As the stress concentration region expands, these localized stresses propagate layer by layer along the load-bearing struts. In the case of RD3, a stress-concentrated band emerges at a 45° angle to the Z-axis, indicating that these load-bearing struts bear a heavier load and accumulate more energy. Consequently, for RD3, stress concentrations predominantly occur in the direction of 45° to the Z-axis during compressive deformation. The obvious discrepancies in the failure mode of scaffolds during loading come from the mechanical properties of the parent material together with the designed architecture. As a useful criterion, lattice structures can be classified into two groups based on their failure mode: bending-dominated structures and stretch-dominated structures [22,27,67]. The bending-dominated structure

Table 6
The mechanical features of Ti–6Al–4V scaffolds fabricated by EB-PBF, having different cell types and sizes.

Scaffolds	Yield strength (σ_s-MPa)	First maximum compressive strength (σ_{max} (UCS)-MPa)	Elastic modulus (E-GPa)	$\sigma_{Plateau}$ (MPa)	Densification strain (%)	Absorbed energy up to first failure (W*-kJ)	Microhardness ($HV_{0.1}$)
RD3	56.33 ± 4	68.37 ± 6	1.13 ± 0.03	67.42 ± 4.2	37.14 ± 1	2.33 ± 0.20	325 ± 13
RD5	29.53 ± 1	39.42 ± 3	0.69 ± 0.02	36.12 ± 3.2	58.15 ± 1	1.17 ± 0.10	342 ± 9
DO3	33.38 ± 2	40.13 ± 5	0.61 ± 0.02	34.16 ± 2.1	39.17 ± 2	1.31 ± 0.10	310 ± 17
DO5	23.91 ± 1	26.53 ± 2	0.59 ± 0.01	22.21 ± 2.3	41.14 ± 1	0.52 ± 0.05	326 ± 12

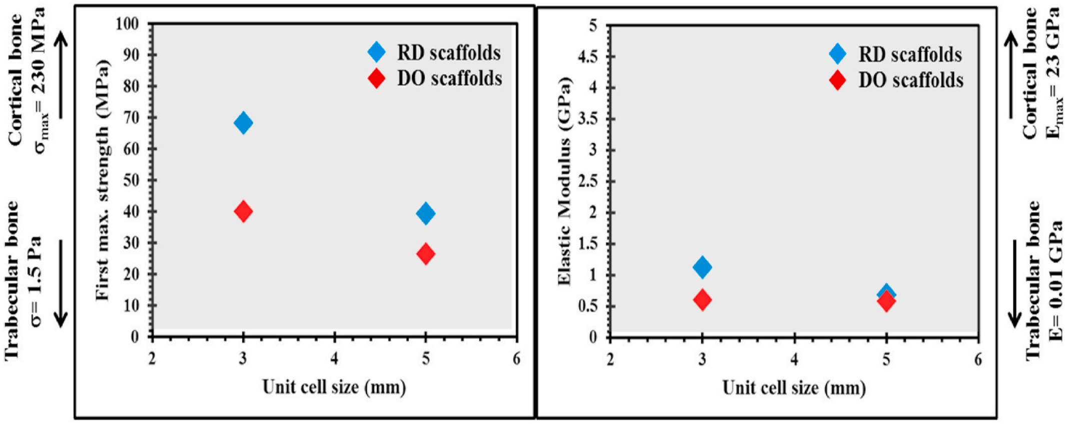

Fig. 9. Comparing the mechanical properties of the EB-PBF Ti–6Al–4V scaffolds and human bone.

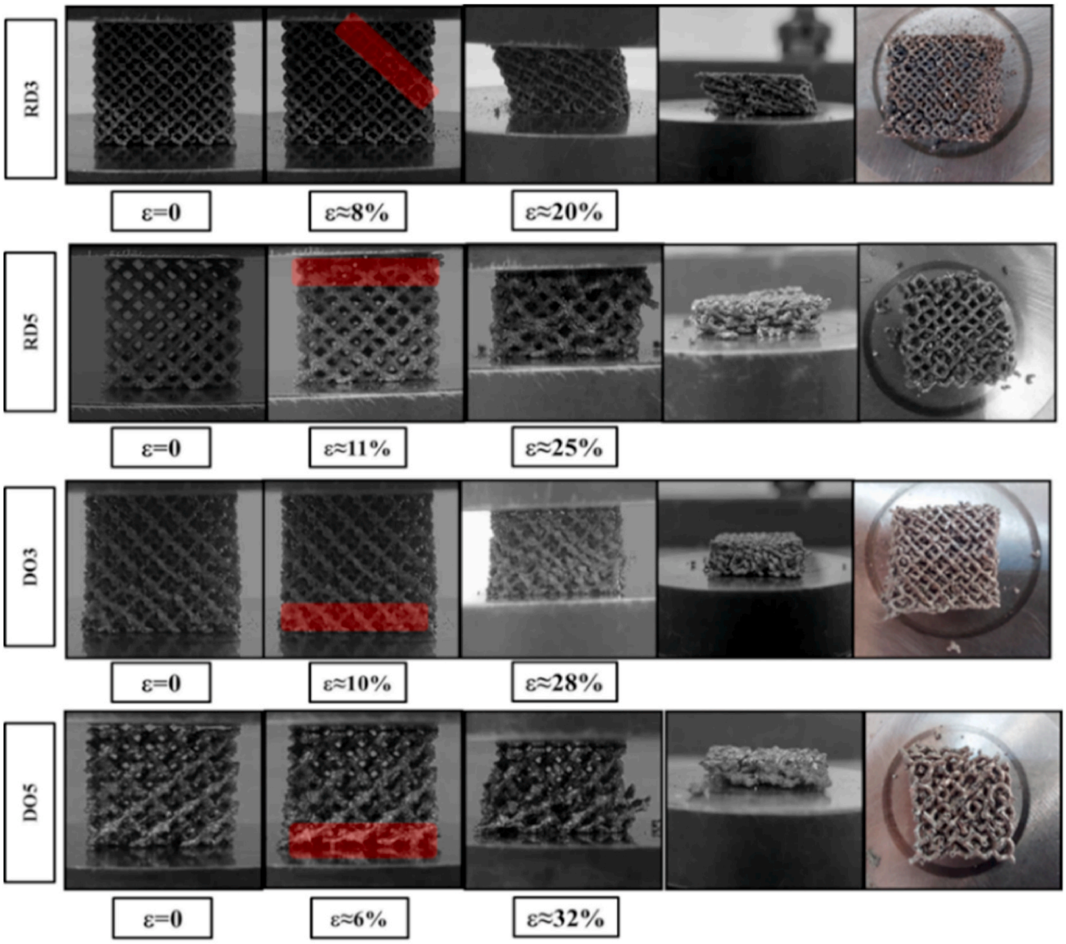

Fig. 10. The visible failure modes at the macroscopic level in EB-PBF Ti–6Al–4V scaffolds.

was detected by the failure accompanied by the shear bands formed at approximately 45° with respect to the compression axis, i.e., the RD3 scaffold, whereas layer-by-layer failure was observed in the stretch-dominated structures, i.e., the RD5, DO3, and DO5. This difference originated from how the micro-struts are placed in relation to the loading direction and their number in the whole structure, which caused the failure type to be different even for the structure with a similar cell type. Indeed, the higher the number of parallel micro-struts (or with a low slope) to the loading direction, the greater the tendency to buckle, resulting in stretch-dominated failure. Whereas, the more the inclination of the micro-struts to the loading direction, the higher the probability of shear failure, leading to the structure experiencing the bending-dominant.

The SEM images of the fracture surfaces of EB-PBF Ti–6Al–4V scaffolds after the compression testing are displayed in Fig. 11.

The fracture surface mostly showed ductile dimple tearing as a sign of ductile fracture, but on some sections of the fracture surface, local quasi-cleavage type fracture was also observed, referring a mixed mode of ductile and brittle fracture. A large population of much finer, deeper, and evenly distributed dimples on the fracture surface suggests that

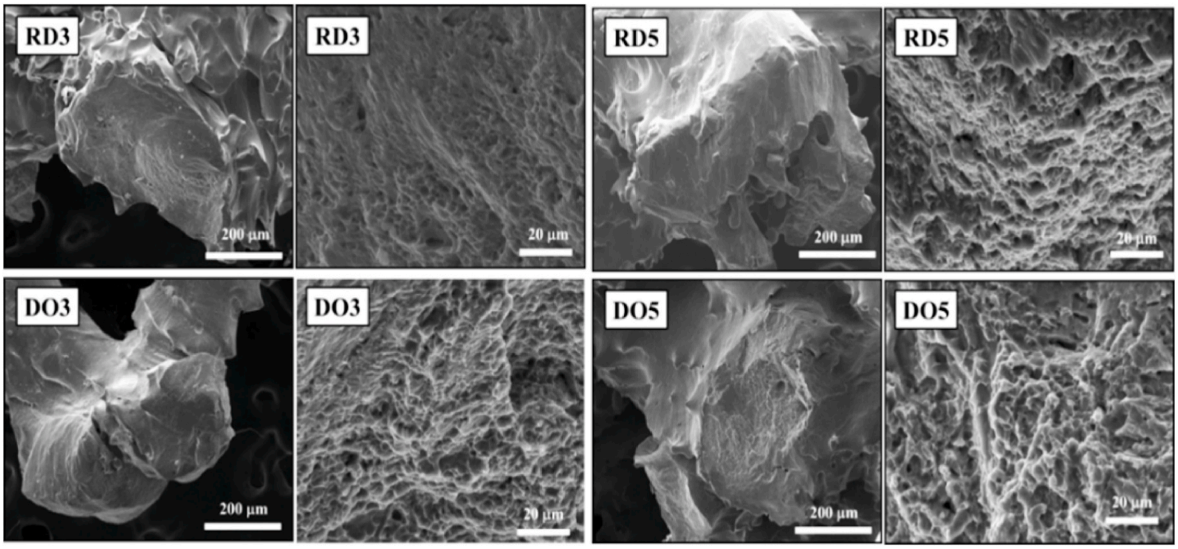

Fig. 11. The SEM images of the fracture surfaces of the EB-PBF Ti–6Al–4V scaffolds after the compression loading.

plastic deformation was significant in the scaffolds. This fracture mode was documented in prior studies on Ti–6Al–4V samples fabricated by EB-PBF [6,47].

3.5. Wettability and permeability of Ti–6Al–4V scaffolds

For biomedical applications, the surface wettability of scaffolds plays a critical role in cell adhesion and proliferation behaviour [19,68]. In

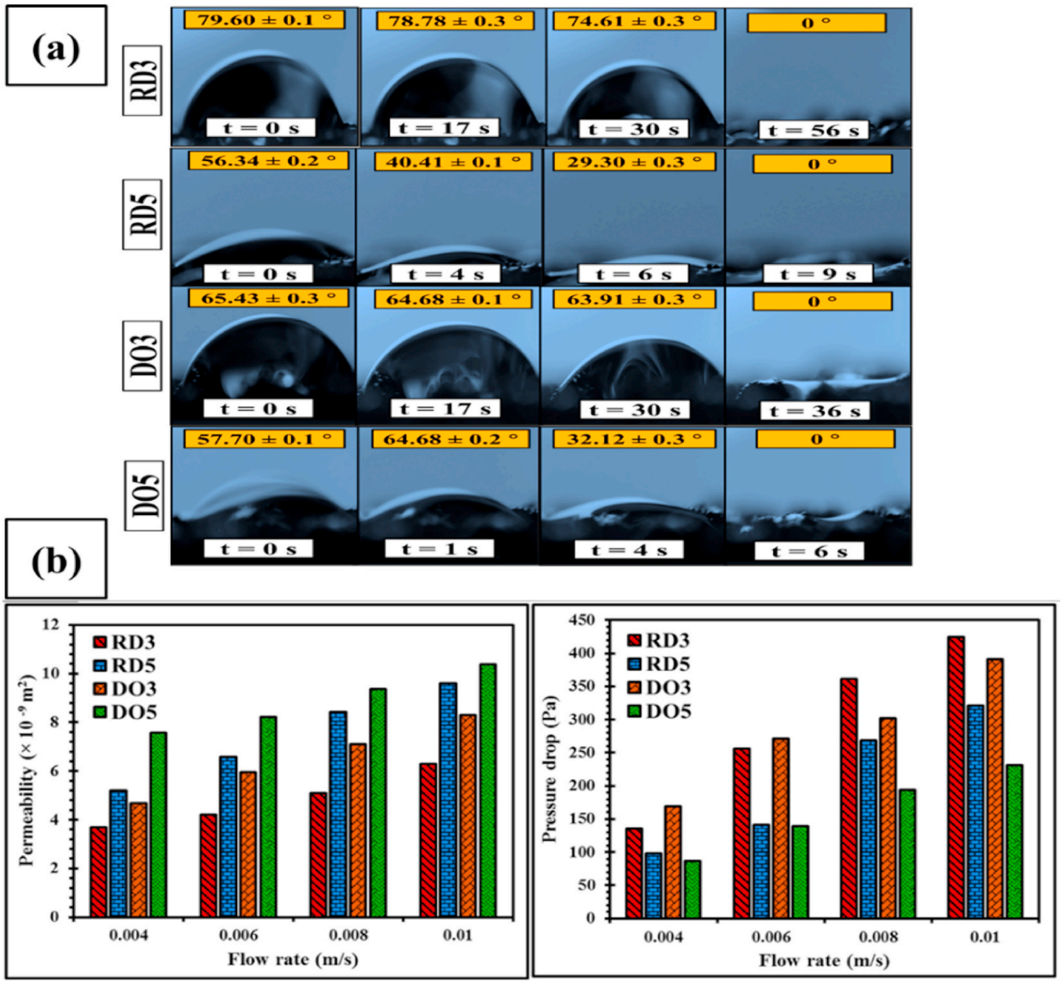

Fig. 12. (a) Time-lapse images of the dynamic wetting behaviour of the EB-PBF Ti–6Al–4V scaffolds and (b) the average pressure drop and permeability of the EB-PBF Ti–6Al–4V scaffolds versus the flow rate.

the present study, the pore size was designed to be large enough to mimic the mechanical properties of bone by the scaffold as much as possible by reducing the elastic modulus. The initial droplet deposition on the surface of the scaffold alone is not an accurate criterion for the wettability of these scaffolds. Accordingly, the contact angle at the first moment ($\theta_{t=0}$), the residence time of the drop on the surface (Δt), and contact angle variation versus time were particularly interesting only to compare the scaffold's wettability. As shown in Fig. 12 (a), time-lapse imaging confirmed that the cell type had no strong effect on the dynamic wettability, whereas increasing the cell size significantly reduced the wettability. The parameters related to the dynamic wettability of the scaffolds are listed in Table 7. Permeability plays a crucial role in scaffolds, directly impacting their interaction with surrounding biological tissues. It refers to the scaffold's ability to allow the passage of fluids, gases, and nutrients. Proper permeability is vital because it influences biocompatibility, tissue integration, cellular function, and the overall success and longevity of the implant. When scaffolds have optimal permeability, they facilitate the flow of essential substances, creating a conducive environment for tissue integration and minimizing the risk of inflammation or rejection. Such well-designed scaffolds contribute to a harmonious interaction with the biological environment, promoting healing and enhancing overall performance [37,69–71]. Pore size and surface area, as two contradictory parameters, are the most important factors in the biological behaviour of the scaffolds in terms of cell adhesion and transportation of nutrients into the scaffold. The larger pore size is suitable for enhancing the permeability of scaffolds and thus improving the delivery of nutrients into the scaffold. The larger the surface area, the better are the cell adhesion and proliferation [37]. According to the Kozeny-Carman equation [72], a traditional permeability–porosity relationship, porosity is described as the main factor parameter in determining the permeability of the scaffold, and the surface area is the second place. However, it is revealed that the cell type could play a significant role in the permeability of the scaffolds. Fig. 12 (b) illustrates the pressure drop and permeability characteristics of EB-PBF Ti–6Al–4V scaffolds in relation to flow rate. The results clearly demonstrate that an increase in flow rate, irrespective of cell type or size, led to higher permeability and pressure drop. Furthermore, larger cell sizes correspond to reduced pressure drops and increased permeability when the flow rate remains constant. This suggests a higher internal fluid flow rate, which could enhance the transport of nutrients and facilitate waste material elimination [37].

The sequence of the permeability values for EB-PBF Ti–6Al–4V scaffolds was as follows: DO5 > RD5 > DO3 > RD3. As expected, the permeability enhanced with the increase in cell size (i.e. increase in pore size) for each cell type. Moreover, the permeability is different for the scaffold with different cell types under the same cell size, which can be attributed to the structure complexity. From Table 7, the permeability of DO scaffolds was higher than that of RD scaffolds at the same cell size. This is because as the fluid moves along the flow direction, it encounters more obstacles in the RD structure, which has a more tortuous architectural structure than the DO structure; therefore, fluid flows more smoothly in the RD. These findings implied that the channel size of the structure and the straight path of the fluid streamline from the inlet to the outlet are the first and second factors, respectively, influencing the permeability of scaffolds [37,69–71]. With regard to the results, the permeability values of all the scaffolds were in agreement with those reported for human trabecular bone (5.13×10^{-9} m^2) [37]. Consequently, these kinds of structure designs were proven to be beneficial to better transport of body fluids and stronger biological fixation by facilitating the ingrowth of bone tissue into the interconnected pores of implants, ultimately ensuring good osseointegration and long-term stability.

Table 7
Parameters related to the dynamic wettability and permeability of EB-PBF Ti–6Al–4V scaffolds.

Scaffolds	Contact angle at the first moment ($\theta_{t=0}$-degree)	Residence time of the drop on the surface (Δt-s)	Permeability at flow rate = 0.01 m/s ($\times 10^{-9}$ m^2)
RD3	79.60 ± 0.1	56 ± 4	6.30 ± 0.4
RD5	56.34 ± 0.3	9 ± 0.6	9.59 ± 0.7
DO3	65.43 ± 0.3	33 ± 6	8.31 ± 0.5
DO5	57.70 ± 0.1	6 ± 0.8	10.38 ± 0.8

3.6. *Electrochemical behaviour of Ti–6Al–4V scaffolds*

Corrosion has the potential to release metallic ions into surrounding tissues, which may lead to adverse reactions and inflammation. Ensuring optimal corrosion performance is critical for maintaining scaffold biocompatibility and preserving tissue health. Over time, corrosion can compromise the structural integrity of implants. Therefore, investigating the corrosion performance of the fabricated samples is essential to ensure long-term stability and functionality, ultimately reducing the risk of mechanical failure [30,32,73,74]. Therefore, one of the goals of this study was to explore whether the corrosion performance of the EB-PBF Ti–6Al–4V scaffolds was favourable as a prerequisite factor for implant applications. Fig. 13 represents the E_{OCP} variation as a function of time for the scaffolds in PBS at 37°. E_{OCP} reflects the electrochemical reactions occurring at the scaffolds/PBS interface [29].

As can be observed, for all scaffolds, the potential exhibited an increasing trend towards a nobler potential after being exposed to the PBS until it finally reached a nearly constant value, indicating the formation and growth of a protective oxide film on the surface of the scaffolds over time. Notably, the formation of a passive oxide layer on the surface of Ti-based alloys is responsible for their remarkable corrosion resistance [30,75–77]. The stable E_{OCP} were −14.49, −9.34, −14.78, and −5.20 mV for RD3, RD5, DO3, and DO5 scaffolds, respectively. It is clear that the time to reach the stable potential for the scaffolds with large cell sizes was less than for scaffolds with small cell sizes, which means that the formation of a stable passive layer on their surface was faster [76]. Moreover, all the scaffolds showed almost similar E_{OCP}; however, the E_{OCP} value was slightly more positive for the scaffolds with large cell sizes, confirming their higher thermodynamically stability compared to others. The E_{ocp} fluctuations observed in the E_{OCP}-t curves of RD3 samples can be related to the simultaneous formation and dissolution of its passive layer [30,31]. The potentiodynamic polarization curves of as-built Ti–6Al–4V scaffolds in PBS at 37 °C are shown in Fig. 14.

No significant difference was found in the cathodic branch, confirming a similar cathodic reaction for all the scaffolds in PBS [30,53].

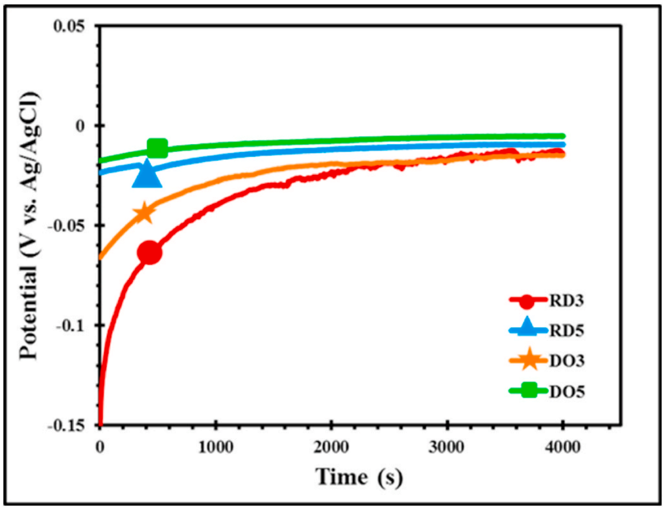

Fig. 13. The OCP curves for EB-PBF Ti–6Al–4V scaffolds.

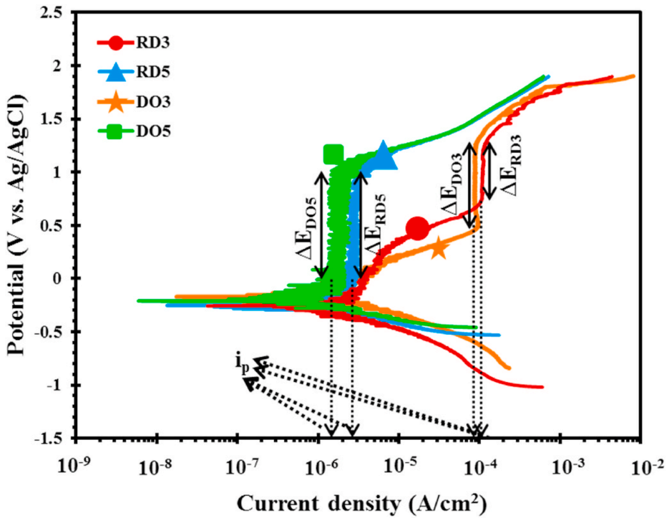

Fig. 14. Potentiodynamic polarization curves depicting the corrosion behaviour of EB-PBF Ti–6Al–4V scaffolds in PBS at 37 °C.

For all the designs on the anodic branch, three distinct regions, including active, passive, and transpassive regions, were observed. Additionally, the anodic slop (β_a) at the active region was far higher than the cathodic slope (β_c), which means that the rate of anodic reactions was more intense than that of the cathodic reactions, attributing to the formation of the protective oxide film. The active region can be influenced by the complex nature of the passive film formed on the Ti alloys, having a relatively porous outer layer and compact inner layer with the protective barrier role. This caused a difference in the active region of the scaffolds [30,76]. Corrosion parameters were derived through the analysis of the potentiodynamic polarization curves and are listed in Table 8.

The more negative E_{corr} value indicates a higher corrosion susceptibility. The passivation potential (E_p), which marks the initiation of the passivation region, is typically inversely correlated with the ease of passivation film formation. The lower the E_p is, the more readily the passivation film is formed. The breakdown potential (E_b) indicates the potential where the passive film begins to breakdown, and a higher E_b represents the higher stability of the passive film formed on the scaffold surface. In this regard, ΔE, i.e. (E_b-E_p), presents the stable passivation region, and a greater ΔE suggests that the passive film is more stable on the surface of scaffolds. The passivation current density (i_p) represents the current at which the stability of the passive film is maintained on the surface, and the lower it is, the lower the dissolution rate of the film [78]. From Table 8, regardless of cell type, the scaffolds exhibited relatively similar corrosion behaviour; whereas the corrosion performance of scaffolds degraded with a decrease in cell size. Namely, with a decrease in cell size for DO scaffolds, the E_{corr} decreased from - 0.23 V to −0.17 V, and the i_{corr} increased from 3.2×10^{-7} A/cm^2 to 17.2×10^{-7} A/cm^2. In general, the inherent tendency of metals is to revert towards their most thermodynamically stable state, which is manifested for Ti–6Al–4V by the formation and growth of a protective oxide film under corrosive conditions [29,30,78]. All the samples exhibited passive film formation as the potential increased towards the passive region. For Ti–6Al–4V alloys in the PBS solution, during the anodic polarization, Ti starts to dissolve in the PBS, and the Ti ions, in the form of Ti^{+4}, enter the solution. At this moment, the current enhances exponentially with the increase in potential, as can be observed on the active region of potentiodynamic polarization curves. Within the PBS medium, Ti^{+4} ions react with H_2O, forming the protective TiO2 film on the scaffold's surface [31]. This protective film covers the surface of the scaffold, playing a vital role in the corrosion inhibition of the scaffolds by preventing the metal from dissolving. With further anodic reactions, the protective film has the potential to envelop the entire metal surface, markedly slowing down the rate of metal dissolution. In the following, metal dissolving ends at the E_p of metal which is proportional to the i_p. At this current, namely the current plateau, it can be seen that the current becomes independent of potential changes [75], indicating that the scaffolds surface was completely covered by a protective passive film. As seen in Fig. 14, the scaffolds with large cell sizes exhibited better passivation behaviour, which is characterized by a greater current plateau region. Findings revealed that the current plateau region of all the scaffolds extended to high anode potentials near 1.5 V. This is due to the fact that the electrode potential is generally low and does not exceed 1.5 V under in-vivo conditions [29]. It can be, therefore, inferred that the EB-PBF Ti–6Al–4V scaffolds can be a good candidate for biomedical applications.

Table 8
The corrosion parameters obtained from polarization curves of EB-PBF Ti–6Al–4V scaffolds in PBS at 37 °C.

Scaffolds	i_{corr} (μA/cm^2)	E_{corr} (V vs. Ag/AgCl)	E_p (V vs. Ag/AgCl)	E_b (V vs. Ag/AgCl)	i_p (μA/cm^2)	ΔE (V vs. Ag/AgCl)
RD3	1.63	−0.37	0.66	1.13	88.30	0.47
RD5	0.58	−0.26	−0.14	0.86	2.24	1
DO3	1.72	−0.17	0.44	1.17	81.90	0.73
DO5	0.32	−0.23	−0.13	1.09	1.14	1.32

The EIS analyses were performed to investigate the electrochemical behaviour s of scaffolds at the scaffold/PBS interfaces. Nyquist and Bode plots of EB-PBF Ti–6Al–4V scaffolds in PBS at 37 °C are depicted in Fig. 15(a–c).

Nyquist plots showed incomplete and distorted capacitive semicircles for all the scaffolds in the whole frequency range. Clearly, it can be found that the cell type had no significant effects on the impedance loop, whereas with a decrease in cell size, the diameter of the semicircle reduced. This trend indicates that the corrosion resistance of the scaffolds decreased. The capacitive semicircles are associated with the dielectric properties of the oxide film that spontaneously developed on the scaffold's surface [75]. The Bode plots represent the change in the absolute value of the impedance and the phase angle as a function of the logarithm of the frequency [30]. Two distinct regions can be distinguished in the plot of log |Z| against log f, where in the frequency range of 10^2–10^5 Hz (high frequencies), the impedance curves exhibited a slope near zero, and, at medium and low frequencies (10^{-2}-10^2 Hz), the impedance curves demonstrated a linear pattern with an approximate slope of −1. Additionally, for all the scaffolds, according to the phase angle vs. log f plot, at high frequencies, the phase shift between current and voltage approached 0°, where the electrolyte resistance (R_s) is dominant in determining the total impedance. At low frequencies, the maximum phase angle was observed at about −80°, attributing to the dielectric characteristics of the protective oxide film developed on the surface of the scaffolds, and it reflects the capacitive behaviour of the electrode [29,30,79]. Therefore, the impedance of all the scaffolds was enhanced with the exposure time to PBS. Additionally, it can be found that the frequency range of the maximum phase angle for the scaffolds with small cell size was narrower than that of the scaffolds with large cell size, demonstrating that the decrease in cell size reduced the stability of the passive layer on the surface of scaffolds. The equivalent circuit model applied to analyze EIS data is shown in Fig. 15 (d), and the fitting parameters are listed in Table 9.

The equivalent circuit of the scaffolds consists of the R_s, corresponding to the solution resistance, in series with two-time constants. Both time constants are made of the parallel connection of the constant phase element (CPE) and the resistance. In this scheme, it is accepted that the oxide layer formed on the scaffolds' surface consists of two layers, including a barrier inner layer (CPE_b/R_b) and a porous outer layer (CPE_p/R_p), corresponding to those previously suggested for Ti-based alloys [53,75]. In the fitted equivalent circuit, the first-time constants (CPE_p/R_p) described the properties of the outer porous oxide

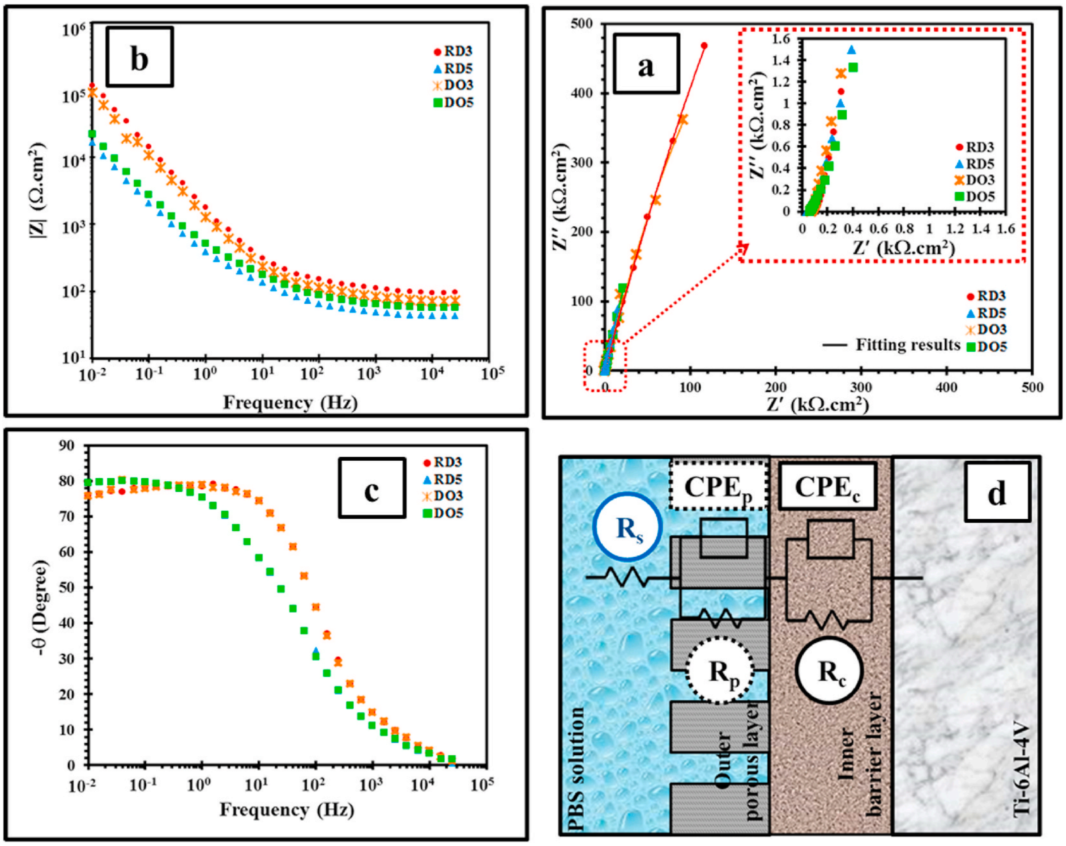

Fig. 15. EIS spectra of EB-PBF Ti–6Al–4V scaffolds in PBS at 37 °C: (a) Nyquist plots, (b, c) Bode plots, (d) the equivalent electric circuit.

Table 9
EIS fitting results of the EB-PBF Ti–6Al–4V scaffolds in PBS at 37 °C.

Scaffolds	R_s ($\Omega.cm^2$)	R_p ($\Omega.cm^2$)	CPE_p ($\Omega^{-1}.cm^{-2}.S^n$)	n_1	R_b ($\Omega.cm^2$)	CPE_b ($\Omega^{-1}.cm^{-2}.S^n$)	n_2	χ^2
RD3	71.32	21.38	2.79×10^{-5}	0.85	4.73×10^6	2.95×10^{-5}	0.88	0.0004
RD5	54.67	271.80	8.39×10^{-4}	0.55	5.54×10^6	9.91×10^{-5}	0.90	0.0002
DO3	94.42	29.49	2.71×10^{-5}	0.82	5.73×10^6	2.38×10^{-5}	0.88	0.0009
DO5	41.68	182.30	9.20×10^{-5}	0.56	6.28×10^6	13.09×10^{-5}	0.90	0.0003

film, and the second-time constants (CPE_b/R_b) represented the inner barrier oxide film. CPE_b and R_b represent the capacity and the resistance of the inner barrier film, respectively, and CPE_p is the capacity, and R_p is the resistance of the outer porous film. It is worth noting that, herein, the outcomes showed a deviation from the ideal behaviour, for example, the Bode's slope was not exactly equal to −1, originating from the roughness of the surface of the electrode and inhomogeneities in the oxide film. Therefore, CPE is employed as a substitute for an ideal capacitor, whose impedance (Z_{CPE}) is characterized as follows [30];

$$Z_{CPE} = [Q(j\omega)^n]^{-1} \tag{5}$$

where Q represents a frequency-independent constant and is attributed to the surface condition. n is the exponent of a CPE and ranges from −1 to +1. CPE represents a pure resistor for $n = 0$, an inductor for $n = -1$, and a capacitance for $n = +1$. ω and j are the circular frequency of the alternating current (AC) signal ($\omega = 2\pi f$) and imaginary number ($j = \sqrt{-1}$), respectively. The fitting error, represented by the sum of chi-squared (χ^2), was less than 2×10^{-4}, which confirmed that quite a good fit was achieved for EIS data. From Tables 9 and it can be seen that, for all the scaffolds, the inner barrier layer exhibited extremely high resistance, whereas the outer porous layer had significantly lower resistance. This indicated that the inner oxide film played a main role in preventing further metal dissolution in the first few days of exposure to PBS. For the inner film, the value of n_2 was closer to 1, showing a relatively ideal capacitive behaviour for the inner layer. In general, results indicated that, in PBS, the cell type had little effect on the electrochemical behaviour of EB-PBF Ti–6Al–4V scaffolds. However, it is revealed that the smaller cell size led to the degradation of corrosion resistance. Several reasons can be proposed for the higher corrosion rate of the scaffolds with small cell sizes, to mention a few. (i) The larger the exposed surface area, the greater the electrochemical reactions between the PBS electrolyte and the Ti–6Al–4V scaffolds, leading to a higher corrosion rate [30]. Considering that the scaffolds with small cell sizes have a larger surface area than the others, it can be argued that the corrosion rate of scaffolds with small cell sizes was higher. (ii) It is clear that the geometrical structure of the scaffolds with small cell sizes is more complex than those with large cell sizes because the pore size is very small, and the struts are very close together. As a result, the PBS solution may hardly flow inside such a complex structure, assisting the trapping of the electrolyte ions and promoting the exhaustion of oxygen supply, which in turn resulted in the formation of a thin passive layer and the decrease in corrosion resistance. This is while electrolytes flow easily throughout the scaffolds with large cell sizes, replenishing the oxygen supply during the passivation process and avoiding the change in microenvironment concentration. Thereby, this helps to minimize the risk of corrosion of scaffolds [30]. (iii) It is known that in Ti alloys, β phase is more capable of forming a more stable protective oxide film than (phase). Moreover, in the dual α/β phase, the finer the structure is, the more likely it is to form a galvanic cell at the α/β interface, ultimately accelerating the corrosion rate [53,80]. As the scaffolds with large cell sizes not only have a high volume fraction of β phase but also exhibit a coarser structure, they can be expected to show better corrosion resistance.

The corrosion behaviour of all the scaffolds was also monitored by EIS analysis on day 21 after immersion in PBS at 37 °C. As can be seen in Fig. 16, the corrosion behaviour of the scaffolds on day 21 was almost the same as the behaviour of those on day 1, suggesting that the corrosion resistance did not significantly change with the increase in immersion time in PBS. This is a sign of the high stability of the oxide films after long-term immersion of the scaffolds in PBS. Notably, the equivalent circuit utilized to analyze the impedance data on day 21 was similar to that on day 1, and the fitting parameters are listed in Table 10.

Titanium and vanadium release from the scaffolds were measured after immersion for 21 days in PBS at 37 °C, as shown in Fig. 17. It can be seen that the total release of Ti and V ions was enhanced with the increase in immersion time (Fig. 17 (a and b).

In return, Fig. 17 (c and d), which presents the average content of Ti and V release per day derived from statistical analysis, disclosed the ion release gradually decreased from day 1 to day 14 and reached an almost constant value on day 14 for all the scaffolds. This means that the macroscopic corrosion rate of the scaffolds in PBS gradually decreased over immersion time. These findings showed that the cell type did not have much effect on the ion release, and the decrease in cell size increased ion release from EB-PBF Ti–6Al–4V scaffolds in PBS to some extent. The reasons for that have already been rehearsed above. It is important to recognize that while the surface chemistry of biomaterials fundamentally influences ion release, the surface area significantly magnifies this impact. A larger surface area offers more sites for interaction between the scaffold material and the surrounding biological environment. This heightened interaction increases the likelihood of ion

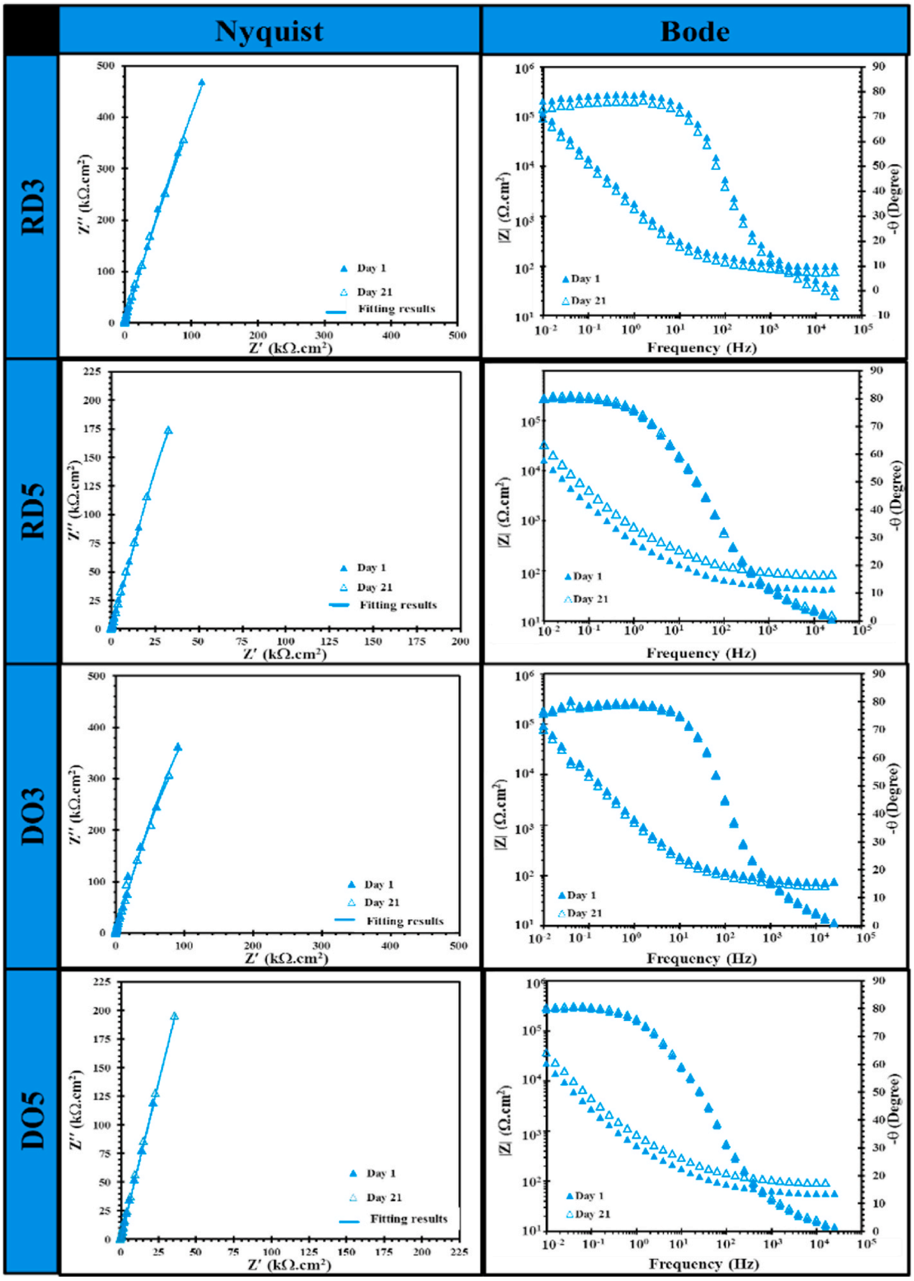

Fig. 16. Comparison of EIS results of EB-PBF Ti–6Al–4V scaffolds in PBS solution at 37 °C after days 1 and 21.

Table 10
EIS fitting results of EB-PBF Ti–6Al–4V scaffolds in PBS at 37 °C on day 21.

Scaffolds	R_s ($\Omega.cm^2$)	R_p ($\Omega.cm^2$)	CPE_p ($\Omega^{-1}.cm^{-2}.S^n$)	n_1	R_b ($\Omega.cm^2$)	CPE_b ($\Omega^{-1}.cm^{-2}.S^n$)	n_2	X^2
RD3	71.76	22.41	3.75×10^{-5}	0.82	4.36×10^{6}	2.40×10^{-5}	0.88	0.0009
RD5	80.43	414.10	4.66×10^{-4}	0.53	7.63×10^{6}	6.75×10^{-5}	0.90	0.0003
DO3	59.95	19.45	4.29×10^{-5}	0.81	4.02×10^{6}	3.46×10^{-5}	0.89	0.0009
DO5	89.20	470.70	1.94×10^{-4}	0.55	7.79×10^{6}	6.03×10^{-5}	0.90	0.0002

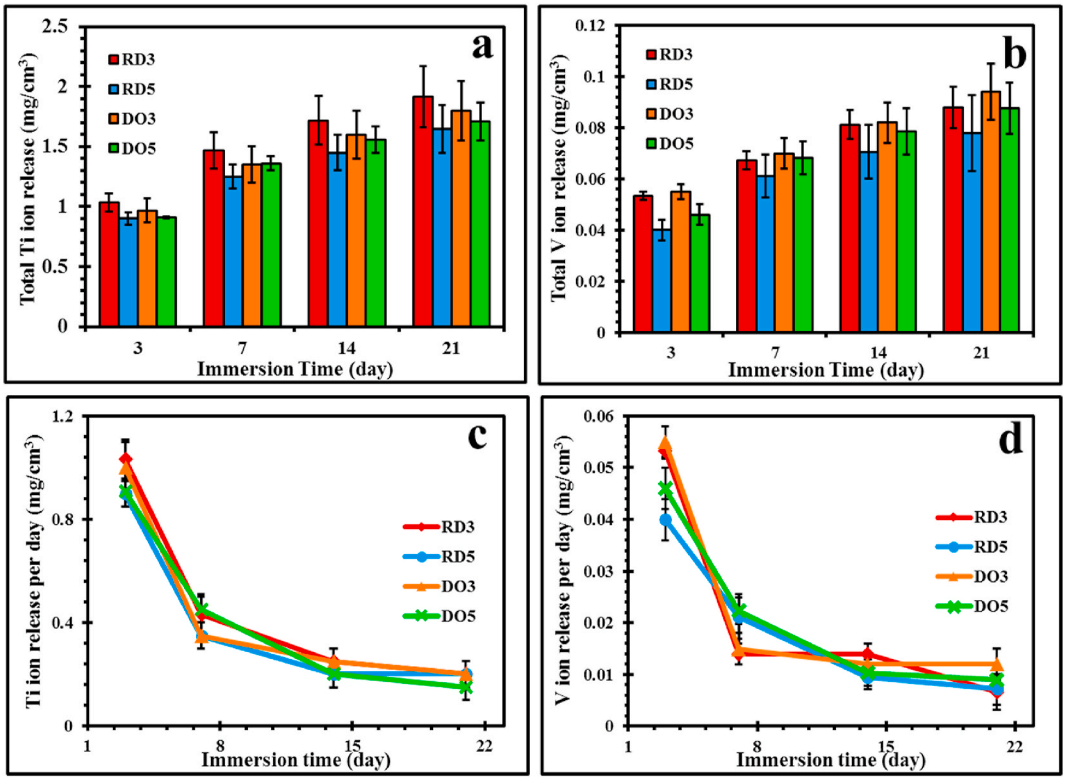

Fig. 17. The ion release of EB-PBF Ti–6Al–4V scaffolds in PBS solution at 37 °C versus time: (a) the total release of Ti, (b) the total release of V, (c) the release of Ti per day, (d) the release of V per day.

release from the scaffold. Furthermore, a greater surface area exposes more material to the corrosive effects of bodily fluids, potentially leading to increased corrosion and the subsequent release of ions from the scaffold material [81,82].

4. Conclusions

In the current study, the effects of cell type and cell size on the performance of Ti–6Al–4V scaffolds fabricated via EB-PBF were investigated in detail. For this purpose, diamond (DO) and rhombic dodecahedron (RD) cell type-based scaffolds with various cell sizes were designed and fabricated by the EB-PBF process. The scaffolds were characterized from the perspective of application aspects, including the microstructural and mechanical properties, permeability, and short/long-term corrosion behaviour for orthopaedic implants. Our findings are outlined as follows.

1 Chemical etching, as a post-processing stage, plays an effective role in removing surface defects and improving the surface quality of scaffolds. Herein, optimal etching time is crucial depending on the cell type and size; in larger cells, less etching time is required regardless of the cell type.
2 The microstructure of all the scaffolds consisted of a dual α/β phase, almost similar for the same cell size, irrespective of cell type. The β spacing increases with an increase in the cell size (i.e. thicker struts). As the cell size increases, the resulting microstructure becomes coarser.
3 Mechanical characterization indicated that the RD scaffolds exhibited higher mechanical properties at the same cell size as DI scaffolds regarding elastic modulus, yield stress and first maximum compressive strength. With the increase in cell size, the mechanical strength of the scaffold decreased, but all scaffolds were mechanically qualified for orthopaedic implant applications.
4 The permeability values of EB-PBF Ti–6Al–4V scaffolds, which are compatible with the permeability of human trabecular bone, are in the order of DO5 > RD5 > DO3 > RD3. RD structure has a more tortuous architectural structure than the DO structure; therefore, fluid flows more slowly and encounters more obstacles in the RD structure. The permeability increases with the increase in cell size (i.e. increase in pore size), regardless of cell type.
5 The cell type experiences little effect on the corrosion behaviour of the scaffolds. For both cell types, as the cell size decreases, the scaffolds exhibit an inferior corrosion resistance in PBS solution, mainly relating to the greater surface area exposed to the electrolyte, more α/β interfaces, and lower volume fraction of β phase. The corrosion resistance does not significantly change with the increase in immersion time in PBS. The ion release of Ti and V from the scaffolds gradually decreases, approaching an almost constant value after a certain time (on day 14) for the scaffolds.

Declaration of competing interest

The authors declare that they have no known competing financial interests or personal relationships that could have appeared to influence the work reported in this paper.

References

[1] Aufa AN, Hassan MZ, Ismail Z. Recent advances in Ti-6Al-4V additively manufactured by selective laser melting for biomedical implants: Prospect development. J Alloys Compd 2022;896:163072. https://doi.org/10.1016/j.jallcom.2021.163072.

[2] Guddati S, Kiran ASK, Leavy M, Ramakrishna S. Recent advancements in additive manufacturing technologies for porous material applications. Int J Adv Manuf Technol 2019;105:193–215. https://doi.org/10.1007/s00170-019-04116-z.

[3] Mosallanejad MH, Abdi A, Karpasand F, Nassiri N, Iuliano L, Saboori A. Additive manufacturing of titanium alloys; Processability, properties and applications. Adv Eng Mater 2023:1–29. 2301122.

[4] Galati M, Gatto ML, Bloise N, Fassina L, Saboori A, Visai L, et al. Biocompatibility of Ti-48Al-2Cr-2Nb produced by electron beam powder bed fusion (EB-PBF). Mater Today Proc 2022;70:483–6. https://doi.org/10.1016/J.MATPR.2022.09.466.

[5] Taghian M, Mosallanejad MH, Lannunziata E, Del Greco G, Iuliano L, Saboori A. Laser powder bed fusion of metallic components: latest progress in productivity, quality, and cost perspectives. J Mater Res Technol 2023;27:6484–500. https://doi.org/10.1016/j.jmrt.2023.11.049.

[6] Ataee A, Li Y, Fraser D, Song G, Wen C. Anisotropic Ti-6Al-4V gyroid scaffolds manufactured by electron beam melting (EBM) for bone implant applications. Mater Des 2018;137:345–54. https://doi.org/10.1016/j.matdes.2017.10.040.

[7] Del Guercio G, Galati M, Saboori A. Innovative approach to evaluate the mechanical performance of Ti–6Al–4V lattice structures produced by electron beam melting process. Met Mater Int 2021;27:55–67. https://doi.org/10.1007/s12540-020-00745-2.

[8] Del Guercio G, Galati M, Saboori A. Electron beam melting of Ti-6Al-4V lattice structures: correlation between post heat treatment and mechanical properties. Int J Adv Manuf Technol 2021;116:3535–47. https://doi.org/10.1007/s00170-021-07619-w.

[9] Del Guercio G, Galati M, Saboori A, Fino P, Iuliano L. Microstructure and mechanical performance of Ti–6Al–4V lattice structures manufactured via electron beam melting (EBM): a review. Acta Metall Sin (English Lett 2020;33:183–203. https://doi.org/10.1007/s40195-020-00998-1.

[10] Mosallanejad MH, Niroumand B, Ghibaudo C, Biamino S, Salmi A, Fino P, et al. In-situ alloying of a fine grained fully equiaxed Ti-based alloy via electron beam powder bed fusion additive manufacturing process. Addit Manuf 2022;56:102878. https://doi.org/10.1016/j.addma.2022.102878.

[11] Wang X, Xu S, Zhou S, Xu W, Leary M, Choong P, et al. Topological design and additive manufacturing of porous metals for bone scaffolds and orthopaedic implants: a review. Biomaterials 2016;83:127–41. https://doi.org/10.1016/j.biomaterials.2016.01.012.

[12] Song C, Liu L, Deng Z, Lei H, Yuan F, Yang Y, et al. Research progress on the design and performance of porous titanium alloy bone implants. J Mater Res Technol 2023;23:2626–41. https://doi.org/10.1016/j.jmrt.2023.01.155.

[13] Koptyug A, Khrapov D, Surmeneva M, Surmenev R. Triply periodic minimal surfaces manufactured by electron beam powder bed fusion: approaches and challenges. Key Eng Mater 2023;964:91–6. https://doi.org/10.4028/p-gguN5j.

[14] Yánez A, Cuadrado A, Martel O, Afonso H, Monopoli D. Gyroid porous titanium structures: a versatile solution to be used as scaffolds in bone defect reconstruction. Mater Des 2018;140:21–9. https://doi.org/10.1016/j.matdes.2017.11.050.

[15] Khrapov D, Kozadayeva M, Manabaev K, Panin A, Sjöström W, Koptyug A, et al. Different approaches for manufacturing ti-6al-4v alloy with triply periodic minimal surface sheet-based structures by electron beam melting. Materials 2021;14. https://doi.org/10.3390/ma14174912.

[16] Polley C, Radlof W, Hauschulz F, Benz C, Sander M, Seitz H. Morphological and mechanical characterisation of three-dimensional gyroid structures fabricated by electron beam melting for the use as a porous biomaterial. J Mech Behav Biomed Mater 2022;125. https://doi.org/10.1016/j.jmbbm.2021.104882.

[17] Zumofen L, Kopanska KS, Bono E, Kirchheim A, De Haller EB, Graf-Hausner U. Properties of additive-manufactured open porous titanium structures for patient-specific load-bearing implants. Front Mech Eng 2022;7. https://doi.org/10.3389/fmech.2021.830126.

[18] Liu F, Zhang DZ, Zhang P, Zhao M, Jafar S. Mechanical properties of optimized diamond lattice structure for bone scaffolds fabricated via selective laser melting. Materials 2018;11. https://doi.org/10.3390/ma11030374.

[19] Huang G, Pan ST, Qiu JX. The clinical application of porous tantalum and its new development for bone tissue engineering. Materials 2021;14. https://doi.org/10.3390/ma14102647.

[20] Bai L, Yi C, Chen X, Sun Y. Effective design of the graded strut of BCC lattice. Materials 2019;12. https://doi.org/10.3390/ma12132192.

[21] Liu Z, Gong H, Gao J, Liu L. Topological design, mechanical responses and mass transport characteristics of high strength-high permeability TPMS-based scaffolds. Int J Mech Sci 2022;217. https://doi.org/10.1016/j.ijmecsci.2021.107023.

[22] Benedetti M, du Plessis A, Ritchie RO, Dallago M, Razavi SMJ, Berto F. Architected cellular materials: a review on their mechanical properties towards fatigue-tolerant design and fabrication. Mater Sci Eng R Rep 2021;144:100606. https://doi.org/10.1016/j.mser.2021.100606.

[23] Liu L, Wang S, Liu J, Deng F, Li Z, Hao Y. Architectural design of Ti6Al4V scaffold controls the osteogenic volume and application area of the scaffold. J Mater Res Technol 2020;9:15849–61. https://doi.org/10.1016/j.jmrt.2020.11.061.

[24] Goto M, Matsumine A, Yamaguchi S, Takahashi H, Akeda K, Nakamura T, et al. Osteoconductivity of bioactive Ti-6Al-4V implants with lattice-shaped interconnected large pores fabricated by electron beam melting. J Biomater Appl 2021;35:1153–67. https://doi.org/10.1177/0885328220968218.

[25] Chang B, Song W, Han T, Yan J, Li F, Zhao L, et al. Influence of pore size of porous titanium fabricated by vacuum diffusion bonding of titanium meshes on cell penetration and bone ingrowth. Acta Biomater 2016;33:311–21. https://doi.org/10.1016/j.actbio.2016.01.022.

[26] Wang P, Li X, Luo S, Nai MLS, Ding J, Wei J. Additively manufactured heterogeneously porous metallic bone with biostructural functions and bone-like mechanical properties. J Mater Sci Technol 2021;62:173–9. https://doi.org/10.1016/j.jmst.2020.05.056.

[27] Zhang XY, Fang G, Zhou J. Additively manufactured scaffolds for bone tissue engineering and the prediction of their mechanical behavior: a review. Materials 2017;10. https://doi.org/10.3390/ma10010050.

[28] Galati M, Saboori A, Biamino S, Calignano F, Lombardi M, Marchiandi G, et al. Ti-6Al-4V lattice structures produced by EBM: heat treatment and mechanical properties. Procedia CIRP 2020;88:411–6. https://doi.org/10.1016/j.procir.2020.05.071.

[29] Zhao B, Wang H, Qiao N, Wang C, Hu M. Corrosion resistance characteristics of a Ti-6Al-4V alloy scaffold that is fabricated by electron beam melting and selective laser melting for implantation in vivo. Mater Sci Eng C 2017;70:832–41. https://doi.org/10.1016/j.msec.2016.07.045.

[30] Gai X, Liu R, Bai Y, Li S, Yang Y, Wang S, et al. Electrochemical behavior of open-cellular structured Ti-6Al-4V alloy fabricated by electron beam melting in simulated physiological fluid: the significance of pore characteristics. J Mater Sci Technol 2022;97:272–82. https://doi.org/10.1016/j.jmst.2021.05.024.

[31] Gai X, Bai Y, Li S, Hou W, Hao Y, Zhang X, et al. In-situ monitoring of the electrochemical behavior of cellular structured biomedical Ti-6Al-4V alloy fabricated by electron beam melting in simulated physiological fluid. Acta Biomater 2020;106:387–95. https://doi.org/10.1016/j.actbio.2020.02.008.

[32] Romero-Resendiz L, Rossi MC, Álvarez A, García-García A, Milián L, Tormo-Más M, et al. Microstructural, mechanical, electrochemical, and biological studies of an electron beam melted Ti-6Al-4V alloy. Mater Today Commun 2022;31. https://doi.org/10.1016/j.mtcomm.2022.103337.

[33] Xu W, Yu A, Jiang Y, Li Y, Zhang C, Singh H, et al. Gyroid-based functionally graded porous titanium scaffolds for dental application: design, simulation and characterizations. Mater Des 2022;224:111300. https://doi.org/10.1016/j.matdes.2022.111300.

[34] Liang CY, Jiang XJ, Ji RL, Li BE, Zou XR, Wang HS, et al. Preparation and surface modification of 3D printed Ti–6Al–4V porous implant. Rare Met 2021;40:1164–72. https://doi.org/10.1007/s12598-020-01413-5.

[35] Naghavi SA, Wang H, Varma SN, Tamaddon M, Marghoub A, Galbraith R, et al. On the morphological deviation in additive manufacturing of porous Ti-6Al-4V scaffold: a design consideration. Materials 2022;15. https://doi.org/10.3390/ma15144729.

[36] Sokollu B, Gulcan O, Konukseven EI. Mechanical properties comparison of strut-based and triply periodic minimal surface lattice structures produced by electron beam melting. Addit Manuf 2022:60. https://doi.org/10.1016/j.addma.2022.103199.

[37] Yu G, Li Z, Li S, Zhang Q, Hua Y, Liu H, et al. The select of internal architecture for porous Ti alloy scaffold: a compromise between mechanical properties and permeability. Mater Des 2020;192. https://doi.org/10.1016/j.matdes.2020.108754.

[38] Zhang L, Song B, Yang L, Shi Y. Tailored mechanical response and mass transport characteristic of selective laser melted porous metallic biomaterials for bone scaffolds. Acta Biomater 2020;112:298–315. https://doi.org/10.1016/j.actbio.2020.05.038.

[39] Takezawa A, Yonekura K, Koizumi Y, Zhang X, Kitamura M. Isotropic Ti-6Al-4V lattice via topology optimization and electron-beam melting. Addit Manuf 2018;22:634–42. https://doi.org/10.1016/j.addma.2018.06.008.

[40] Downing D, Leary M, McMillan M, Alghamdi A, Brandt M. Heat transfer in lattice structures during metal additive manufacturing: numerical exploration of temperature field evolution. Rapid Prototyp J 2020;26:911–28. https://doi.org/10.1108/RPJ-11-2018-0288.

[41] Safdar A, He HZ, Wei LY, Snis A, Chavez De Paz LE. Effect of process parameters settings and thickness on surface roughness of EBM produced Ti-6Al-4V. Rapid Prototyp J 2012;18:401–8. https://doi.org/10.1108/13552541211250391.

[42] de Damborenea JJ, Arenas MA, Larosa MA, Jardini AL, de Carvalho Zavaglia CA, Conde A. Corrosion of Ti-6Al-4V pins produced by direct metal laser sintering. Appl Surf Sci 2017;393:340–7. https://doi.org/10.1016/j.apsusc.2016.10.031.

[43] de Formanoir C, Suard M, Dendievel R, Martin G, Godet S. Improving the mechanical efficiency of electron beam melted titanium lattice structures by chemical etching. Addit Manuf 2016;11:71–6.

[44] Chen C, Hao Y, Bai X, Ni J, Chung SM, Liu F, et al. 3D printed porous Ti-6Al-4V cage: effects of additive angle on surface properties and biocompatibility; bone ingrowth in Beagle tibia model. Mater Des 2019;175. https://doi.org/10.1016/j.matdes.2019.107824.

[45] Carolo L CB, Cooper O RE. A review on the influence of process variables on the surface roughness of Ti-6Al-4V by electron beam powder bed fusion. Addit Manuf 2022;59:103103. https://doi.org/10.1016/J.ADDMA.2022.103103.

[46] Soro N, Saintier N, Attar H, Dargusch MS. Surface and morphological modification of selectively laser melted titanium lattices using a chemical post treatment. Surf

Coatings Technol 2020;393:125794. https://doi.org/10.1016/j.surfcoat.2020.125794.

[47] Rafi HK, Karthik NV, Gong H, Starr TL, Stucker BE. Microstructures and mechanical properties of Ti-6Al-4V parts fabricated by selective laser melting and electron beam melting. J Mater Eng Perform 2013;22:3872–83. https://doi.org/10.1007/s11665-013-0658-0.

[48] Haubrich J, Gussone J, Barriobero-Vila P, Kürnsteiner P, Jägle EA, Raabe D, et al. The role of lattice defects, element partitioning and intrinsic heat effects on the microstructure in selective laser melted Ti-6Al-4V. Acta Mater 2019;167:136–48. https://doi.org/10.1016/j.actamat.2019.01.039.

[49] Dietrich K, Diller J, Dubiez-Le Goff S, Bauer D, Forêt P, Witt G. The influence of oxygen on the chemical composition and mechanical properties of Ti-6Al-4V during laser powder bed fusion (L-PBF). Addit Manuf 2020;32. https://doi.org/10.1016/j.addma.2019.100980.

[50] Cardon A, Mareau C, Ayed Y, Van Der Veen S, Giraud E, Philippe Dal S. Heat treatment simulation of Ti-6Al-4V parts produced by selective laser melting. Addit Manuf 2021;39:101766. https://doi.org/10.1016/j.addma.2020.101766.

[51] Iliana J of MR and T, Mohd F, Ahmad M, Bakar A, Afiqah N, Radzuan M, et al. Influence of heat treatment parameters on microstructure and mechanical performance of titanium alloy in LPBF : a brief review. J Mater Res Technol 2023;24:4091–110. https://doi.org/10.1016/j.jmrt.2023.04.090.

[52] Zhou X, Xu D, Geng S, Fan Y, Liu M, Wang Q, et al. Mechanical properties, corrosion behavior and cytotoxicity of Ti-6Al-4V alloy fabricated by laser metal deposition. Mater Charact 2021:179. https://doi.org/10.1016/j.matchar.2021.111302.

[53] Szymczyk-Ziółkowska P, Hoppe V, Gąsiorek J, Rusińska M, Kęszycki D, Ł Szczepański, et al. Corrosion resistance characteristics of a Ti-6Al-4V ELI alloy fabricated by electron beam melting after the applied post-process treatment methods. Biocybern Biomed Eng 2021;41:1575–88. https://doi.org/10.1016/j.bbe.2021.10.002.

[54] Carrozza A, Marchese G, Saboori A, Bassini E, Aversa A, Bondioli F, et al. Effect of aging and cooling path on the super Β-transus heat-treated Ti-6Al-4V alloy produced via electron beam melting (EBM). Materials 2022;15:4067. https://doi.org/10.3390/ma15124067.

[55] Toh WQ, Wang P, Tan X, Nai MLS, Liu E, Tor SB. Microstructure and wear properties of electron beam melted Ti-6Al-4V parts: a comparison study against as-cast form. Metals 2016;6. https://doi.org/10.3390/met6110284.

[56] Tan X, Kok Y, Tan YJ, Descoins M, Mangelinck D, Tor SB, et al. Graded microstructure and mechanical properties of additive manufactured Ti–6Al–4V via electron beam melting. Acta Mater 2015;97:1–16. https://doi.org/10.1016/j.actamat.2015.06.036.

[57] Silvestri AT, Foglia S, Borrelli R, Franchitti S, Pirozzi C, Astarita A. Electron beam melting of Ti6Al4V: role of the process parameters under the same energy density. J Manuf Process 2020;60:162–79. https://doi.org/10.1016/j.jmapro.2020.10.065.

[58] Castany P, Pettinari-Sturmel F, Crestou J, Douin J, Coujou A. Experimental study of dislocation mobility in a Ti-6Al-4V alloy. Acta Mater 2007;55:6284–91. https://doi.org/10.1016/j.actamat.2007.07.032.

[59] Yan X, Li Q, Yin S, Chen Z, Jenkins R, Chen C, et al. Mechanical and in vitro study of an isotropic Ti-6Al-4V lattice structure fabricated using selective laser melting. J Alloys Compd 2019;782:209–23. https://doi.org/10.1016/j.jallcom.2018.12.220.

[60] Cheng XY, Li SJ, Murr LE, Zhang ZB, Hao YL, Yang R, et al. Compression deformation behavior of Ti-6Al-4V alloy with cellular structures fabricated by electron beam melting. J Mech Behav Biomed Mater 2012;16:153–62. https://doi.org/10.1016/j.jmbbm.2012.10.005.

[61] Yang E, Leary M, Lozanovski B, Downing D, Mazur M, Sarker A, et al. Effect of geometry on the mechanical properties of Ti-6Al-4V Gyroid structures fabricated via SLM: a numerical study. Mater Des 2019;184:108165. https://doi.org/10.1016/j.matdes.2019.108165.

[62] Zhang XZ, Leary M, Tang HP, Song T, Qian M. Selective electron beam manufactured Ti-6Al-4V lattice structures for orthopedic implant applications: current status and outstanding challenges. Curr Opin Solid State Mater Sci 2018;22:75–99. https://doi.org/10.1016/j.cossms.2018.05.002.

[63] Marin E, Fusi S, Pressacco M, Paussa L, Fedrizzi L. Characterization of cellular solids in Ti-6Al-4V for orthopaedic implant applications: trabecular titanium. J Mech Behav Biomed Mater 2010;3:373–81. https://doi.org/10.1016/j.jmbbm.2010.02.001.

[64] Zhang XY, Yan XC, Fang G, Liu M. Biomechanical influence of structural variation strategies on functionally graded scaffolds constructed with triply periodic minimal surface. Addit Manuf 2020;32. https://doi.org/10.1016/j.addma.2019.101015.

[65] Tan X, Kok Y, Tan YJ, Vastola G, Pei QX, Zhang G, et al. An experimental and simulation study on build thickness dependent microstructure for electron beam melted Ti-6Al-4V. J Alloys Compd 2015;646:303–9. https://doi.org/10.1016/j.jallcom.2015.05.178.

[66] Razavi SMJ, Van Hooreweder B, Berto F. Effect of build thickness and geometry on quasi-static and fatigue behavior of Ti-6Al-4V produced by electron beam belting. Addit Manuf 2020;36. https://doi.org/10.1016/j.addma.2020.101426.

[67] Yu G, Li X, Dai L, Xiao L, Song W. Compressive properties of imperfect Ti-6Al-4V lattice structure fabricated by electron beam powder bed fusion under static and dynamic loadings. Addit Manuf 2022;49. https://doi.org/10.1016/j.addma.2021.102497.

[68] Demirci S, Dalmış R, Dikici T, Tünçay MM, Kaya N, Güllüoğlu AN. Effect of surface modifications of additively manufactured Ti-6Al-4V alloys on apatite formation ability for biomedical applications. J Alloys Compd 2021;887:161445. https://doi.org/10.1016/j.jallcom.2021.161445.

[69] Shi C, Lu N, Qin Y, Liu M, Li H, Li H. Study on mechanical properties and permeability of elliptical porous scaffold based on the SLM manufactured medical Ti-6Al-4V. PLoS One 2021;16. https://doi.org/10.1371/journal.pone.0247764.

[70] Montazerian H, Zhianmanesh M, Davoodi E, Milani AS, Hoorfar M. Longitudinal and radial permeability analysis of additively manufactured porous scaffolds: effect of pore shape and porosity. Mater Des 2017;122:146–56. https://doi.org/10.1016/j.matdes.2017.03.006.

[71] Karuna C, Poltue T, Khrueaduangkham S, Promoppatum P. Mechanical and fluid characteristics of triply periodic minimal surface bone scaffolds under various functionally graded strategies. J Comput Des Eng 2022;9:1258–78. https://doi.org/10.1093/jcde/qwac052.

[72] Goetzendorfer B, Kirchgaessner H, Hellmann R. Tunable, anisotropic permeability and spatial flow of SLM manufactured structures. Materials 2021;14. https://doi.org/10.3390/ma14185205.

[73] Bandekhoda MR, Mosallanejad MH, Atapour M, Iuliano L, Saboori A. Investigation on the potential of laser and electron beam additively manufactured Ti–6Al–4V components for orthopedic applications. Met Mater Int 2023. https://doi.org/10.1007/s12540-023-01496-6.

[74] Atapour M, Wang X, Färnlund K, Odnevall Wallinder I, Hedberg Y. Corrosion and metal release investigations of selective laser melted 316L stainless steel in a synthetic physiological fluid containing proteins and in diluted hydrochloric acid. Electrochim Acta 2020;354:136748. https://doi.org/10.1016/j.electacta.2020.136748.

[75] Gudić S, Vrsalović L, Kvrgić D, Nagode A. Electrochemical behaviour of Ti and Ti-6Al-4V alloy in phosphate buffered saline solution. Materials 2021;14. https://doi.org/10.3390/ma14247495.

[76] Bocchetta P, Chen LY, Tardelli JDC, Dos Reis AC, Almeraya-Calderón F, Leo P. Passive layers and corrosion resistance of biomedical Ti-6Al-4V and β-ti alloys. Coatings 2021;11. https://doi.org/10.3390/coatings11050487.

[77] Mosallanejad MH, Sanaei S, Atapour M, Niroumand B, Iuliano L, Saboori A. Microstructure and corrosion properties of CP-Ti processed by laser powder bed fusion under similar energy densities. Acta Metall Sin (English Lett 2022. https://doi.org/10.1007/s40195-022-01376-9.

[78] Chen LY, Zhang HY, Zheng C, Yang HY, Qin P, Zhao C, et al. Corrosion behavior and characteristics of passive films of laser powder bed fusion produced Ti–6Al–4V in dynamic Hank's solution. Mater Des 2021:208. https://doi.org/10.1016/j.matdes.2021.109907.

[79] Berbel LO, Banczek E do P, Karousis IK, Kotsakis GA, Costa I. Determinants of corrosion resistance of Ti-6Al-4V alloy dental implants in an in vitro model of peri-implant inflammation. PLoS One 2019;14. https://doi.org/10.1371/journal.pone.0210530.

[80] Hemmasian A, Zeng C, Guo S, Raush J. Corrosion behavior of additively manufactured Ti-6Al-4V parts and the effect of post annealing. Addit Manuf 2019;28:252–8. https://doi.org/10.1016/j.addma.2019.05.011.

[81] Myakinin A, Turlybekuly A, Pogrebnjak A, Mirek A, Bechelany M, Liubchak I, et al. In vitro evaluation of electrochemically bioactivated Ti6Al4V 3D porous scaffolds. Mater Sci Eng C 2021;121:111870. https://doi.org/10.1016/j.msec.2021.111870.

[82] Ødegaard KS, Westhrin M, Afif A Bin, Ma Q, Mela P, Standal T, et al. The effects of surface treatments on electron beam melted Ti-6Al-4V disks on osteogenesis of human mesenchymal stromal cells. Biomater Adv 2023;147:213327. https://doi.org/10.1016/j.bioadv.2023.213327.